



VCU

Virginia Commonwealth University
VCU Scholars Compass

Theses and Dissertations


Graduate School

2016

Resolution of Inflammation Rescues Axon Initial Segment Disruption

Nicholas M. George
Virginia Commonwealth University

Follow this and additional works at: <https://scholarscompass.vcu.edu/etd>

 Part of the [Biochemistry, Biophysics, and Structural Biology Commons](#), [Biology Commons](#), [Cell and Developmental Biology Commons](#), [Immunology and Infectious Disease Commons](#), [Medicine and Health Sciences Commons](#), and the [Neuroscience and Neurobiology Commons](#)

© The Author

Downloaded from

<https://scholarscompass.vcu.edu/etd/4186>

This Thesis is brought to you for free and open access by the Graduate School at VCU Scholars Compass. It has been accepted for inclusion in Theses and Dissertations by an authorized administrator of VCU Scholars Compass. For more information, please contact libcompass@vcu.edu.

Resolution of Inflammation Rescues Axon Initial Segment Disruption

A thesis submitted in partial fulfillment of the requirements for the degree of
Master of Science at Virginia Commonwealth University

By

Nicholas Matthew George

Bachelor of Science, Virginia Tech, 2012

Director: Jeffrey L. Dupree, Ph.D.
Associate Professor of Anatomy and Neurobiology

Virginia Commonwealth University
Richmond, Virginia
April 2016

Acknowledgement

I want to first thank my advisor and mentor, Dr. Jeffrey Dupree, for his support, guidance and patience over the last two years. Under his instruction I learned what it means to think critically about my work and perform hypothesis driven science. I will always be grateful to him for teaching me what it means to perform good science, and I hope to continue developing as both a scientist and a mentor using him as an example.

I would like to thank Dr. Unsong Oh and Dr. George H. DeVries for agreeing to serve on my committee and helping to guide and shape this project into what it is today.

I want to sincerely thank the members of the Dupree Lab for their help and support over the past two years. Kareem Clark and Savannah Benusa in particular, I could not have done this without your help. Thank you for your patience and willingness to go above and beyond to teach me and humor my questions. Also, a big thanks to Brooke Sword, who rode in snowstorms with me to take care of the animals. Thank you to everyone else I worked with in the Dupree Lab for making the lab seem like home and for letting me be part of your work. I am lucky to have worked with such awesome scientists and friends.

Finally, I want to thank my family who continues to support me through my extended education and humor my eclectic interests. I love you all and would not be where I am without your love and support.

Table of Contents

Acknowledgement.....	ii
List of Figures.....	v
List of Tables.....	vi
Abbreviations.....	vii
Abstract.....	ix
CHAPTER 1: Introduction.....	1
Neuronal Domains: Somatodendritic Domain	2
Neuronal Domains: Axonal Domain.....	4
Axonal Domain: The node of Ranvier	4
Axonal Domain: The Axon Initial Segment.....	5
Pathology of the AIS.....	15
Hypothesis	22
CHAPTER 2: Materials and Methods	24
Animals.....	24
EAE Induction.....	24
Chronic EAE Didox Treatment	30
LPS-mediated Inflammation.....	30
Immunocytochemistry	32
Microscopy and Image Quantification.....	36
Western Blots	42
Quantitative Reverse Transcriptase Polymerase Chain Reaction (qRT-PCR)	46
Statistical Analysis.....	50
Chapter 3: Chronic EAE Results	51
AIS numbers are reduced in Chronic EAE	51
AIS Length is not different in Late and Chronic EAE.....	53
Neuron cell count is not changed in Late or Chronic EAE.....	53
Microglia display a less reactive morphology in Chronic EAE	55
Inflammatory markers TNFα and iNOS are increased in the EAE Cortex	57
βIV spectrin protein levels are not altered in EAE.....	61
Chapter 4: LPS Induced Inflammation Results.....	63
LPS-mediated inflammation induces AIS shortening and loss which recovers at a chronic time point.....	63
Microglia display a less reactive morphology in 2 Week LPS animals.....	66
Neuron cell count is not changed in LPS-mediated inflammation.....	68
Chapter 5: Discussion	70
Changes in AIS number are observed in Chronic EAE, but these changes are not significant.	70
Initial segments spontaneously recover in LPS-mediated inflammation	70
Microglia become less reactive in Prolonged Inflammation	71
Loss of The Axon Initial Segment in Prolonged Inflammation is Reversible.	73
Chapter 6: Automated Quantitation of Initial Segments and NeuN+ Cells.....	75
Automating Image Processing and Quantitation.....	75

Preprocessing.....	75
Quantitation.....	78
Limitations and Conclusions	84
List of References.....	86
Vita.....	96

List of Figures

Figure 1. The neuron and neuronal domains.....	3
Figure 2. AIS degeneration in MS.....	17
Figure 3. EAE experimental design.....	28
Figure 4. LPS experimental design.....	40
Figure 5. AIS Number and Length in Chronic EAE.....	52
Figure 6. NeuN+ nuclei loss is not detected in Chronic EAE.....	54
Figure 7. Microglia reactivity in Chronic EAE.....	56
Figure 8. TNF α mRNA levels are significantly increased in the cortex of Chronic EAE Mice.....	58
Figure 9. iNOS mRNA levels are elevated in the cortex of Chronic EAE mice.....	59
Figure 10. iNOS protein levels are not changed in Chronic EAE mice.....	60
Figure 11. β IV spectrin protein levels are not changed in Chronic EAE mice.....	62
Figure 12. LPS-mediated inflammation induces significant loss of AIS number and length.....	65
Figure 13. Microglia reactivity in LPS-mediated inflammation.....	67
Figure 14. NeuN+ Nuclei loss is not detected in LPS-mediated inflammation.....	69
Figure 15. <i>SplitChannelMacro</i> explained.....	77
Figure 16. Macro and settings for automated quantitation.....	80
Figure 17. Procedure for automated image quantitation.....	82
Figure 18. No difference is detected between automated counting method and manual counting.....	83

List of Tables

Table 1. Clinical scoring criteria.....	26
Table 2. EAE exclusion criteria.....	29
Table 3. Zeiss LSM 710 microscope settings for chronic EAE study.....	38
Table 4. Zeiss LSM 710 microscope settings for LPS-induced inflammation study.....	40
Table 5. qRT-PCR primer sequences.....	49

Abbreviations

MS-- Multiple Sclerosis

CNS-- Central Nervous System

GFP-- Green Fluorescent Protein

AIS--Axon initial segment

EAE-- Experimental autoimmune encephalomyelitis

IFN- γ -- Interferon- γ

IL-- Interleukin

LPS-- Lipopolysaccharide

Carboxy-- carboxymethylcellulose

Didox-- 3,4-dihydroxybenzohydroxamic acid

PBS-- Phosphate Buffered Saline (Concentration 1X, composition described in Methods)

PIC-- Protease inhibitor cocktail

IBA1-- Ionized calcium binding protein-1

ANOVA-- Analysis of variance

GAPDH-- Glyceraldehyde phosphate dehydrogenase

NIH-- National Institutes of Health

qRT-PCR-- Quantitative reverse transcriptase polymerase chain reaction

Na_v--Voltage gated sodium channel.

L1 CAM-- L1 family of cellular adhesion molecules

PSD-95-- Post-synaptic density-95

iNOS-- Inducible nitric oxide synthase

TNF α -- Tumor necrosis factor alpha

NeuN-- Neuronal nuclei

TLR-- Toll like receptor

IgG-- Immunoglobulin g

NFκB-- Nuclear factor kappa B

MOG-- Myelin oligodendrocyte glycoprotein

CD-- Cluster of differentiation

kD-- kilo Dalton

FIJI-- FIJI is just ImageJ (“Batteries included” distribution of ImageJ)

mV-- millivolt

μm-- micrometer

BLAST-- Basic local alignment search tool

mg-- milligram

Cyclo A-- Cyclophilin A

FOV-- Field of view

Abstract

RESOLUTION OF INFLAMMATION RESCUES AXON INITIAL SEGMENT DISRUPTION

By Nicholas Matthew George, B.S.

A thesis submitted in partial fulfillment of the requirements for the degree of
Master of Science at Virginia Commonwealth University.

Virginia Commonwealth University, 2016.

Major Director: Jeffrey L. Dupree, Ph.D.
Associate Professor of Anatomy and Neurobiology

Axonal domains are required for proper neuron function. These domains are unstable and degenerate concurrent with the inflammation in multiple sclerosis (MS) and the inflammatory disease models experimental autoimmune encephalomyelitis (EAE) and lipopolysaccharide (LPS) induced inflammation. Previous studies from our laboratory have shown that the axon initial segment (AIS) is maintained independently of the presence of myelin, but that AIS disruption is seen in MS as well as EAE and LPS-mediated inflammation. AIS loss can be interrupted in the early stage of EAE using the anti-inflammatory drug Didox. However, the potential for Didox directed repair of the AIS in later stages of disease has not been investigated. Here, we utilize two models of CNS inflammation to assess the possibility of reversing AIS pathology. Based on our findings, we present the first evidence that AIS degeneration, an axonal pathology observed in MS and in chronic inflammation, is reversible.

CHAPTER 1: Introduction

The human brain is a highly complex and segmented collection of around 86 billion cells that function in specialized units to process information and respond to the environment (Azevedo et al., 2009). The complexity and segmented nature of the brain is reflected in the basic cellular unit of the brain: the neuron. Neurons are highly specialized polar cells that can be divided into two primary domains known as the somatodendritic domain and the axonal domain. The proper function of the neuron (and the nervous system as a whole) depends on the formation and maintenance of these domains. Our research focuses on a subdomain of the axon called the Axon Initial Segment (AIS). While structurally very similar to another axonal domain called the node of Ranvier, the initial segment is both formed and maintained in a myelin-independent way (Clark et al., 2016; Hamada and Kole, 2015; Normand and Rasband, 2015). Loss or dysfunction of the AIS has been described in models of stroke (Schafer et al., 2009), schizophrenia (Volk and Lewis, 2005), traumatic brain injury (Baalman et al., 2015) and now in models of multiple sclerosis (Clark et al., 2016). Understanding the processes and mechanisms that regulate the AIS can yield important insights into therapeutic drugs or treatments for diseases that affect it. In this introduction I will explore the broad function of neuronal domains, and then focus on the structure and function of the AIS. I will discuss the major molecular components, the formation, and what is currently known about regulation and maintenance before describing previous results and the hypothesis driving this work.

Neuronal Domains: Somatodendritic Domain

The neuron can be broadly divided into the somatodendritic and axonal domains (Britt et al., 2016) (Figure 1). The somatodendritic domain is the location of the nucleus and is primarily responsible for receiving and integrating synaptic input for propagation in the axonal domain. It contains high concentrations of neurotransmitter receptors, synaptic density proteins like post-synaptic density-95 (PSD-95), and cell adhesion molecules important for synaptic transmission (FarÅas et al., 2012; Horton and Ehlers, 2004).

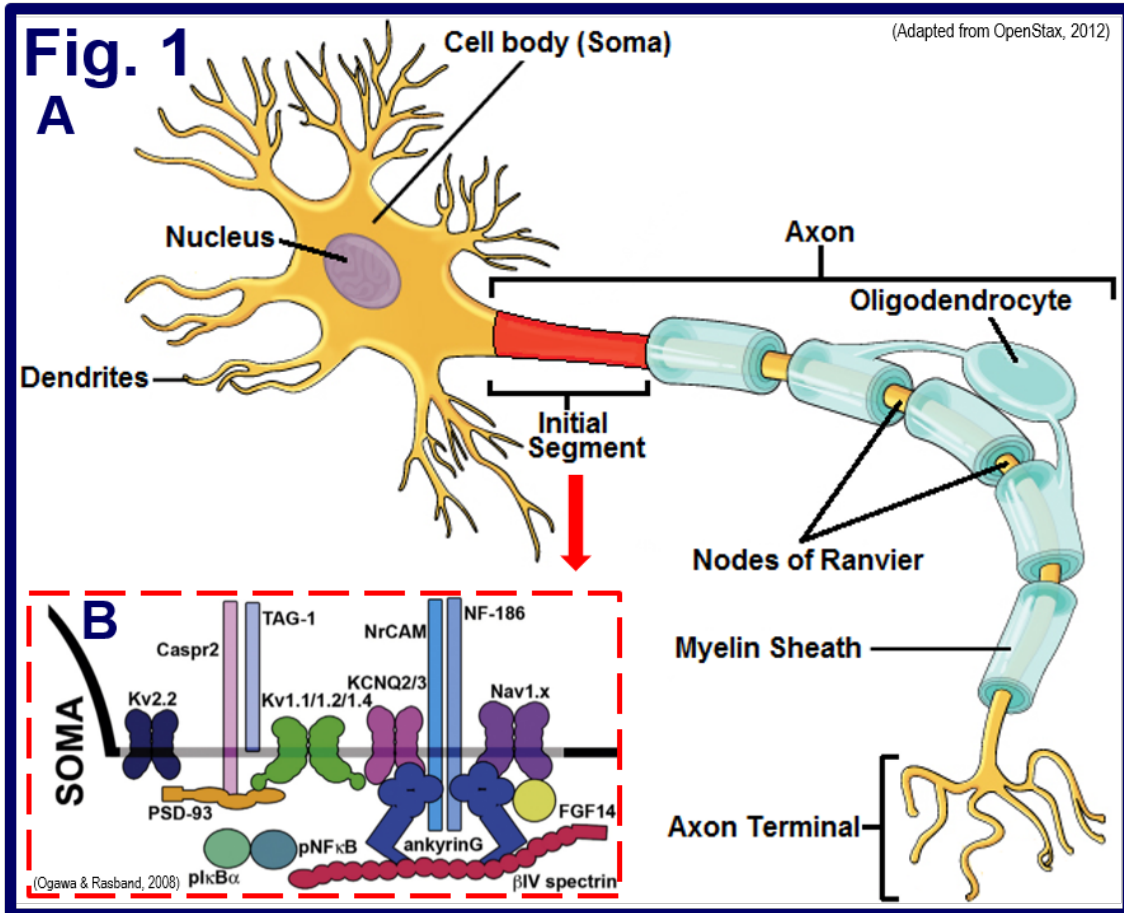


Figure 1. The neuron and neuronal domains. The neuron can be broadly divided into the somatodendritic domain (composed of the dendrites and soma), and the axon (A). The axon itself is divided into sub domains such as the axon initial segment and nodes of Ranvier. The axon initial segment is the portion of the axon immediately distal to the soma and is responsible for initiating action potentials. In myelinated axons, nodes of Ranvier are located between successive myelinated segments of axon. The initial segment and node cluster many similar proteins (B).

Neuronal Domains: Axonal Domain

The axon itself can be subdivided into a number of subdomains based on molecular composition and function. Two vital domains of the axon are the axon initial segment (AIS) and the node of Ranvier. The AIS is located immediately distal to the soma and is responsible for initiating action potentials, while the node of Ranvier exists between segments of myelin and propagates these potentials down the axon. Reflected in their similar roles is a similar molecular composition. The node of Ranvier and AIS cluster many similar molecules, although they are formed and maintained in distinct ways.

Axonal Domain: The node of Ranvier

The node of Ranvier is an electrically active domain of the neuron and myelin is essential for nodal protein clustering. Voltage gated sodium channels (Na_v) are nodal proteins that provide the primary driving force of this electrical activity by allowing sodium ions to pass through the membrane. Early experimenters exploited an in vitro remyelinating model and demonstrated that the process of myelination regulated sodium channel clustering (Vabnick et al., 1996). These results were confirmed in vivo through the use of a demyelinating-remyelinating model, which further demonstrated that sodium channel clustering was dependent on the presence of a myelin sheath (Dupree et al., 2004). More recent work has shown that the myelin protein neurofascin-155 binds the axonal complex of caspr and contactin, resulting in a stable myelin-axon bond and the formation of mechanical barriers that limit lateral movement of the Na_v channels (Susuki and Rasband, 2008). In addition to the myelin sheath, the extracellular matrix and the axonal cytoskeleton also play critical roles in maintaining the node of Ranvier. Neurofascin-186, the neuronal isoform of the neurofascin gene, binds either extracellular matrix proteins or glial proteins, resulting in the stabilization of the node. For example, in the peripheral nervous system,

neurofascin-186 binds the Schwann cell protein gliomedin to stabilize nodal structure (Amor et al., 2014). In addition, neurofascin-186 also assists in assembling and maintaining the node by binding the cytoskeletal scaffolding protein Ankyrin-G. Ankyrin-G in turn anchors Na_v channels in the axonal membrane. Taken together, multiple intrinsic and extrinsic mechanisms work in concert to ensure the structure and function of the node of Ranvier, which is essential for nervous system function.

Axonal Domain: The Axon Initial Segment

As the initiator of action potentials, the AIS contains a complex membrane and cytoplasmic architecture that allows it to generate ionic currents to encode information. As an electrically active domain, the key components of the initial segment includes sodium and potassium channels, and the cellular adhesion molecule Neurofascin-186 on the membrane, as well as the scaffolding protein Ankyrin-G and the cytoskeletal protein β IV spectrin.

Proteins of the Axon Initial Segment

Ankyrin G

Ankyrins are a class of adaptor proteins that link membrane bound ion channels to the spectrin-actin cytoskeleton (Bennett and Baines, 2001; Zhang and Bennett, 1998). There are three main Ankyrin proteins in mammals: Ankyrin-R, Ankyrin-B, and Ankyrin-G. Ankyrin-R is the product of the *ANK1* gene and is primarily found in erythrocytes; Ankyrin-B is broadly expressed and is the product of the gene *ANK2*; Ankyrin-G is the product of *ANK3* and is considered vital to neuronal structure and function (Bennett and Baines, 2001; Kizhatil et al., 2007). Different subtypes of these Ankyrins are produced through alternative splicing, further increasing the diversity of this protein family (Bennett and Baines, 2001).

Generic Ankyrins are composed of a membrane binding domain on the NH₂-terminus containing 24 copies of the 33 residue ANK repeat, a variable-length spectrin binding domain, and a death domain at the C-terminal end (Bennett and Baines, 2001; Kizhatil et al., 2007). Through death domains are known to activate caspase proteases and cell death in other cells, it currently has no known role in Ankyrins (Bennett and Baines, 2001; Mohler et al., 2002). Ankyrin-B and Ankyrin-G are similar in structure and are both found in neurons, although Ankyrin-B is widely dispersed throughout axons and cell bodies while Ankyrin-G is primarily localized at the axon initial segment and nodes of Ranvier (Bennett and Baines, 2001; Kordeli et al., 1995; Zhang and Bennett, 1998). Ankyrin-G is primarily located in the AIS and nodes of Ranvier in the form of a 480 or 270-kD alternatively spliced isoform. These isoforms differ only in the length of a 2300 amino acid unstructured tail (Leterrier, 2016). The localization of Ankyrin-G at the AIS but not Ankyrin-B is thought to come from targeting information in the spectrin binding domain as well as the serine-rich tail domain, which are unique to Ankyrin-G. Evidence suggests that Ankyrin-G accumulates at the initial segment due to exclusion from the distal axon mediated by Ankyrin-B and α II/ β II spectrin, as opposed to direct recruitment by an unidentified receptor (Galiano et al., 2012; Normand and Rasband, 2015).

β IV Spectrin

The primary known role of Ankyrin-G at the initial segment is to bind and localize sodium channels. In order for the Ankyrin-sodium channel structure to be stable and functional, it must also be linked to the actin cytoskeleton. β IV spectrin, a cytoskeletal protein arranged as a hetero-tetramer, serves this role at the initial segment and nodes of Ranvier (Bennett and Baines, 2001; Rasband, 2010). Like Ankyrins, spectrins are a diverse class of molecules. They are composed of α and β subunits, and these subunits undergo differential splicing, further

increasing the diversity. β spectrins have 19 domains: an NH_2 -terminal actin binding domain, 17 triple helical repeat domains (spectrin repeats), and a COOH end with a pleckstrin homology domain (Bennett and Baines, 2001). At the initial segment and nodes of Ranvier, Ankyrin-G binds with βIV spectrin at spectrin repeat 15, which is also necessary for βIV spectrin localization at the AIS (Yang et al., 2007). The binding between Ankyrin-G and βIV spectrin has been shown to be specific to Ankyrin-G, as Ankyrin-B and Ankyrin-R do not co-localize with βIV spectrin as well as Ankyrin-G in immunoprecipitation assays (Yang et al., 2007). βIV spectrin has six alternatively spliced isoforms, but two are localized at initial segments and nodes of Ranvier: βIV spectrin $\Sigma 1$ and βIV spectrin $\Sigma 6$ (Komada and Soriano, 2002; Lacas-Gervais et al., 2004; Yang et al., 2004; Yang et al., 2007).

Neurofascin-186

Along with the cytoskeletal components of the initial segment, Neurofascin-186 of the L1 family of cellular adhesion molecules (L1 CAM) is also present. Neurofascins in particular are important for AIS development, and as previously discussed they are also involved in node of Ranvier development through mediating glial-neuron contact and protein clustering (Davis et al., 1993; Hassel et al., 1997; Sherman et al., 2005). Neurofascin-186 is known to bind Ankyrin-G (Davis et al., 1993) and the importance of Neurofascin-186 at the initial segment is highlighted in conditional knockout mice, which rapidly lose sodium channel labeling within 4 weeks (Zonta et al., 2011).

Sodium Channels

Neurons are electrically active cells that actively maintain a chemical-electrical voltage gradient over its membrane equal to about -70 to -80mV relative to the extracellular environment. Sodium ions are the dominant carrier of charge in vertebrate nervous systems (Castelfranco and Hartline, 2016). For electrically active domains like the AIS and node of Ranvier, voltage gated sodium channels are essential.

Voltage gated sodium channels respond to depolarizing signals that cause the channels to open. When the channels open, sodium ions flow across the membrane and into the neuron due to the chemical (concentration) electrical (-70mV) gradient. This flux of sodium ions causes a temporary flip in membrane potential, which can be propagated along the axon (by opening neighboring sodium channels). This flip in membrane potentials is propagated along an axon and is called the action potential (Castelfranco and Hartline, 2016). The propagation of action potentials is greatly increased in speed by the advent of myelin, the fatty insulation covering a large portion of axons in the vertebrate central and peripheral nervous system. The axon initial segment and node of Ranvier are two unmyelinated segments of the axon, which are involved in the generation and propagation of action potentials (respectively). Not surprisingly, both of these domains contain a density of sodium channels. Although sodium channels are transmembrane proteins, they still require other molecules to anchor them in place in order to properly function. Ankyrins are known to interact with sodium channels through their membrane binding head domain. Sodium channels that are not linked to Ankyrin-G are quickly removed from the membrane via endocytosis (Fache et al., 2004). Specialized sodium channels such as $\text{Na}_v1.6$ are present at the initial segment and nodes along with Ankyrin-G (Bennett and Baines, 2001; Jenkins and Bennett, 2001; Pan et al., 2006; Zhang and Bennett, 1998). $\text{Na}_v1.6$ are not the only

ion channels at the initial segment and node. $\text{Na}_v1.2$, potassium channels, and calcium channels are also present and known to interact with Ankyrin-G at these domains.

Formation of the Axon Initial Segment

The localization of Ankyrin-G at the initial segment and node of Ranvier indicates a vital role at these specialized cellular domains. Early work with the alternatively spliced 480/270 kD Ankyrin-G indicated that it co-localized with sodium channels (Deerinck et al., 1997), Neurofascin, and βIV spectrin (Jenkins and Bennett, 2001; Zhang and Bennett, 1998). Further work by Rasband et al. and others also indicated that Ankyrin-G and βIV spectrin were present at nodes and initial segments and necessary for ion channel localization (Jenkins and Bennett, 2001; Rasband et al., 1999; Zhang and Bennett, 1998). The localization and binding partners emphasize the importance of Ankyrin-G and βIV spectrin to the initial segment. But which protein(s) are responsible for the development of the initial segment?

Work done first by Zhou et al. (1998) and then by Jenkins et al. (2001) with cerebellar specific knockouts of Ankyrin-G supported the idea that Ankyrin-G was the primary initial segment organizer. Zhou et al. (1998) used a cerebellar specific Ankyrin-G knockout mouse and showed that the clustering of both sodium channels and Neurofascin was impaired at the axon initial segment (Zhou et al., 1998). The knockout mice in this study demonstrated clear deficits in action potential initiation and firing. Jenkins and Bennett (2001) also sought to evaluate the possible candidates (L1 CAMs, βIV spectrin, Ankyrin-G) for initial segment organization using the Ankyrin-G knockout mice. They demonstrated that mice lacking Ankyrin-G did not cluster βIV spectrin, Na_v , or L1 CAMs, and did not form functional initial segments in cerebellar Purkinje neurons lacking Ankyrin-G. The symptoms of cerebellar Ankyrin-G knockout mice include tremor, impaired Purkinje neuron firing, and neuronal degeneration. The authors attribute

these symptoms to a loss of sodium channels at the initial segments, likely caused by the lack of Ankyrin-G (Jenkins and Bennett, 2001)

Although the findings of Zhou et al. (1998) and Jenkins and Bennett (2001) demonstrate that Ankyrin-G is an important organizer of the initial segment, Komada and Soriano (2002) developed a mouse carrying a null mutation in the β IV spectrin gene and showed that both Ankyrin-G and sodium channel staining was affected by the loss of β IV spectrin. Using a pan-sodium channel antibody and an anti-Ankyrin-G antibody, they observed only faint labeling for sodium channels and Ankyrin-G when β IV spectrin was absent, which is shown in stark contrast to the uniform localized staining for these proteins at the initial segment of wild type mice (Komada and Soriano, 2002) Symptoms of β IV spectrin mutant mice included tremors and contraction of hind limbs, and these symptoms grew more severe with age. It is interesting to note that while the symptoms of β IV spectrin null animals and cerebellar Ankyrin-G knock out mice both affected movement, the symptoms of the β IV spectrin null mice were less severe than those of the cerebellar specific Ankyrin-G knock out mice (Komada and Soriano, 2002) This could be due to the fact that there were still low levels of Ankyrin-G and Na_v labeling in β IV spectrin mutant mice, whereas this labeling was absent in Ankyrin-G knockout animals.

Yang et al. (2004) showed a similar pattern existed at nodes of Ranvier using the quiver (qv^{3j}) mice, which produced a truncated form of β IV spectrin lacking the pleckstrin homology domain. These mice displayed CNS nodes that were 2X longer than normal nodes and they had striking membrane protrusions when examined under electron microscope (Yang et al., 2004). Later in-vitro studies by Yang et al. (2007) provided evidence that β IV spectrin binds to Ankyrin-G through spectrin repeat 15, and that this repeat is essential to β IV spectrin localization at the initial segment. It was still unclear whether β IV spectrin localized Ankyrin-G

to the AIS or if Ankyrin-G localized β IV spectrin. In order to address this question, Yang et al. (2007) co-transfected cultured hippocampal neurons with green fluorescent protein-labeled Ankyrin-G that was missing the NH₂-terminal membrane-binding domain and Myc-labeled β IV spectrin. This experiment demonstrated that when Ankyrin-G does not have its membrane binding domain, β IV spectrin and Ankyrin-G still bound to one another, but they did not localize at the initial segment. Instead, these protein complexes were spread throughout the cell. The modified Ankyrin-G even had the effect of disrupting the localization of endogenous β IV spectrin. These experiments were initially done with cultured embryonic hippocampal neurons in vitro, but were also replicated in-vivo (Yang et al., 2007).

Taken together, these studies demonstrated the importance of β IV spectrin and Ankyrin-G in the formation and stability of the protein complexes at the initial segment and node of Ranvier, while also singling out Ankyrin-G as the initial organizer. These studies demonstrate why Ankyrin-G has come to be known as the *master organizer* of the AIS (Jenkins and Bennett, 2001; Normand and Rasband, 2015; Sobotzik et al., 2009; Szu-Yu Ho and Rasband, 2011)

Functions and Maintenance

Maintaining Polarity

As previously discussed, neurons are segmented, polarized cells. As well as being the initiator of action potentials, the initial segment also serves as an important barrier between the somatodendritic domain and the axonal domains of the neuron.

Work by Nakada et al. (2003) sought to investigate the presence of a hypothesized membrane diffusion barrier in cultured hippocampal neurons using a fluorescently labeled phospholipid and looking for movement restrictions across the initial segment. If there was restriction of movement at the initial segment, it would be evident by watching this molecule

move across it. Nakada et al. (2003) was able to show that movement was reduced by a factor of about 800 at Ankyrin-G positive axon initial segments, indicating the presence of a barrier to lipid diffusion. This barrier to lipid diffusion only emerged at the initial segment gradually between 1 and 10 days in vitro, with the most dramatic losses in mobility between days 7-10. The diffusion barrier at the membrane was at least partially due to the presence of actin, as depolymerization of fibrous-actin led to increased mobility of lipids at the initial segment. The restriction was then attributed to steric hindrance at the surface due to the accumulation of Ankyrin-G and Na_v complexes at the initial segment, which are anchored to the actin cytoskeleton (Nakada et al., 2003).

Work by Song et al. demonstrated the presence of a cytoplasmic barrier at the initial segment that served as a passive barrier depends on both Ankyrin-G and fibrous-actin by tracking the diffusion of different sized dextrans along the axon (Song et al., 2009). As in previous initial segment barrier experiments (Nakada et al., 2003), Song et al. (2009) noticed the effects of this barrier develop over the course of 3-7 days in vitro; observing almost free diffusion at 3 days in vitro, and markedly reduced movement by 5 days in vitro (Song et al., 2009).

Proteins and Polarity

Once this barrier is set up, it acts as a fence to separate the somatodendritic and axonal domains and keep specialized domain functions occurring in their respective compartments (Rasband, 2010). The proper function of the domains and the neuron as a whole now depends on the presence of this barrier. In a series of experiments performed to investigate the protein components responsible for the maintenance of this fence, Hedstrom et al. (2008) used RNA interference to silence the expression of initial segment proteins in cultured hippocampal

neurons. Silencing experiments were performed on Neurofascin-186, Ankyrin-G, Na_v, and βIV Spectrin. Results indicated that Neurofascin-186, Na_v, and βIV spectrin all had long half-lives and silencing did not greatly affect immunolabeling of these proteins for up to 2 weeks after transfection. However, Ankyrin-G silencing led to a significant loss of Ankyrin-G immunolabeling within 7 days post transfection, and this depletion also led to a dramatic loss of other initial segment proteins (Hedstrom et al., 2008). In order to examine the effects of silencing on neuronal polarity, microtubule associated protein-2 (MAP2), a protein normally restricted to the somatodendritic domain, was immunolabeled 10 days after Ankyrin-G silencing. In untransfected neurons, MAP2 was restricted to the somatodendritic domain with fluorescent intensity decreasing across the initial segment. However, at 10 days post infection, almost all neurons had MAP2 in all visible processes, and processes that were identified as axons based on morphology were found to be positive for the excitatory synapse protein PSD-95, indicating the presence of dendritic spines (Hedstrom et al., 2008). These findings indicated that neuronal polarity had been lost along with the Ankyrin-G.

Using Ankyrin-G knockout mice that also expressed GFP in their Purkinje cells, Sobotzik et al. (2009) investigated axon polarity in the absence of Ankyrin-G in vivo. Purkinje cells were used in these experiments because they have a unique morphology that allows the clear identification of the axon as the long process on the opposite pole of the dendritic tree (Rasband, 2010; Sobotzik et al., 2009). In these mice, the axon formed normally, but close examination of axons in Ankyrin-G knock outs revealed the presence of a number of short protrusions which resemble dendritic spines (Sobotzik et al., 2009). Further examination of these axonal spines indicated that they also contained postsynaptic density proteins common in dendritic spines. 45% of axons in the cerebellar nodule had the unusual spiny phenotype, which was not seen in control

animals (Sobotzik et al., 2009) These results provide evidence that the lack of Ankyrin-G prevents barrier formation between the somatodendritic and axonal domains, causing a dendritic phenotype to develop in the axonal domain in vivo as well as in vitro.

Ankyrin-G is both the master organizer of the initial segment and it also has roles in the maintenance of axonal specificity, making it a particularly vital protein for proper neuron function. Other proteins at the initial segment like Neurofascin-186 and Na_v are important for initial segment function, but have not been shown to be as vital to the integrity of the barrier and functional compartment as Ankyrin-G.

βIV spectrin, while it is not the initial organizer of the AIS, has been shown to be essential to the maintenance and stability of this domain (Komada and Soriano, 2002; Yang et al., 2004; Yang et al., 2007) As previously described, there are two major isoforms of βIV spectrin at the initial segment and nodes of Ranvier, but βIV spectrin $\Sigma 1$ has been shown to be the vital isoform (Lacas-Gervais et al., 2004). When βIV spectrin $\Sigma 1$ is knocked out, mice display nodes that are longer than normal (81% were $>1.5\mu\text{m}$, while only 11% of control mice had nodes $>1.5\mu\text{m}$) and also had abnormal initial segment structure (Lacas-Gervais et al., 2004). Nerve conduction was also negatively affected in these animals, which may explain the quivering phenotype (Lacas-Gervais et al., 2004). βIV spectrin mutants have also been shown to mislocalize Na_v channels at initial segments and nodes of Ranvier, which likely accounts for the quivering symptoms in knockout mice.

Taken together, these studies indicate that βIV Spectrin is important for the long-term stability of the initial segment as opposed to the initial setup. So while Ankyrin-G may be the master organizer, βIV spectrin is also an essential protein required for proper function and stability of the initial segment.

Pathology of the AIS

Multiple Sclerosis

Multiple Sclerosis (MS) is an inflammatory demyelinating disease that affects an estimated 2.3 million people worldwide and is most often diagnosed in adults between the ages of 20-50. It is a wide-ranging disease in terms of symptoms; with vision, balance, gait, and cognition often affected (Anonymous; Minden and Schiffer, 1990). Despite the severity and wide ranging symptoms, the etiology of MS is still largely unknown. The disease is considered immune-mediated and presents with focal demyelination and inflammation of the CNS (Constantinescu et al., 2011; Leray et al., 2010). The devastating effects of MS are colloquially attributed to these demyelinating lesions, but as well as being a demyelinating disease, there is also a significant inflammatory aspect to MS (Constantinescu et al., 2011). In fact, the degree of inflammation closely correlates with disability and is present from the onset of disease and even before demyelination (Bjartmar et al., 2001; Kornek et al., 2000). Bjartmar et al. (2001) has demonstrated that axonal injury occurs in normal appearing white matter before lesions appear in early MS. MS is a disease characterized by both inflammation and demyelination, and they have important consequences for the maintenance of the major functional domains of the axon (Larochelle et al., 2016; Leray et al., 2010).

Although structurally and functionally very similar, the AIS and the node of Ranvier are formed in distinct ways-- with the initial segment being formed intrinsically by the neuron and the nodes of Ranvier depending on glial contact and secreted factors. Another interesting discrepancy in these domains is their responses to disease. In demyelinating models of MS in which an oligodendrocyte toxin is fed to mice and dramatic demyelination is observed, the cluster of proteins that defines a node of Ranvier disperses and can no longer be detected with immunocytochemistry. Upon remyelination, the nodal proteins re-cluster (Dupree et al., 2004). It

has recently been shown that the initial segment does not degenerate following the loss of myelin (Clark et al., 2016; Hamada and Kole, 2015). This discrepancy is interesting in and of itself-- why do these virtually identical domains form in different ways and respond differently to disease? Preliminary evidence from our lab also indicates that the initial segment *does* degenerate in human multiple sclerosis (Figure 2) (Thummala, 2015).

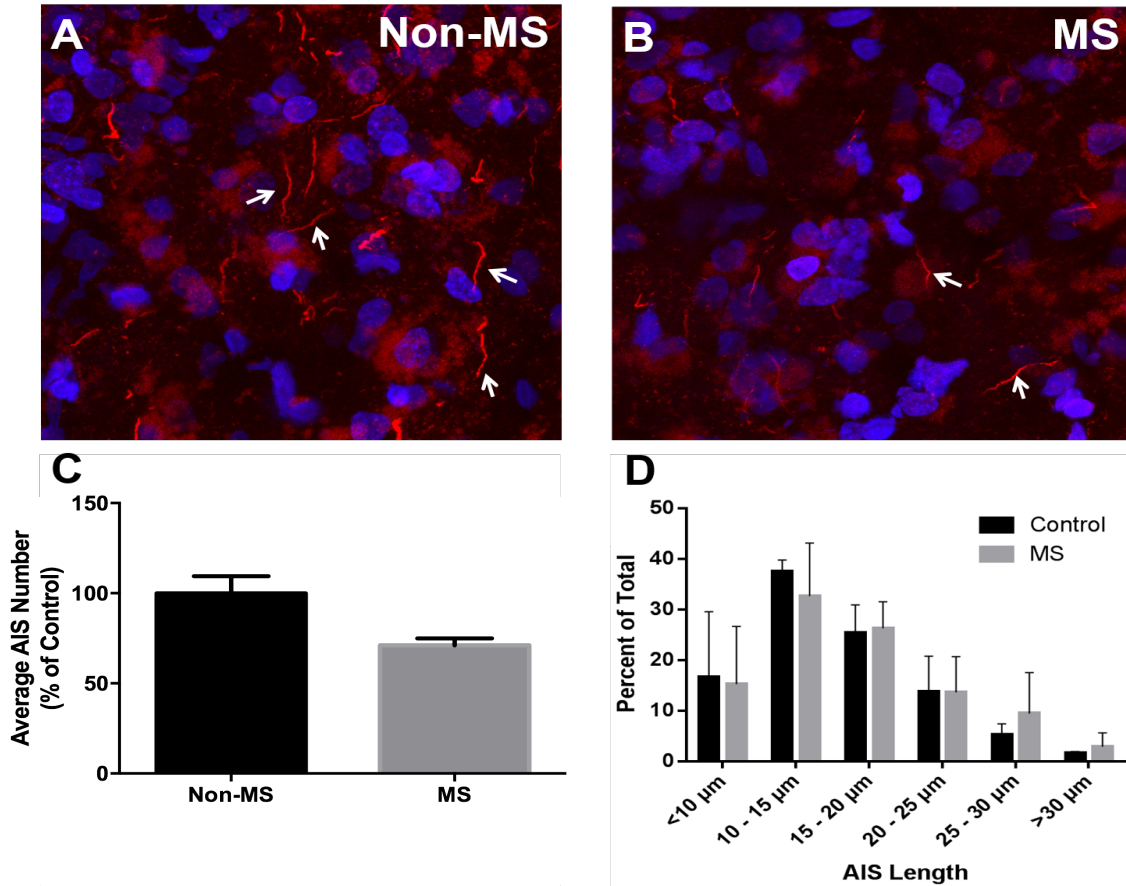


Figure 2. AIS degeneration in MS. Antibodies directed against Ankyrin-G (red, white arrows) robustly label AISs in non-MS brain tissue (A). Although AISs were observed in comparable brain regions from MS brains (B), the number of AISs was reduced in the MS tissue by about 30% (C). Average length of AISs in the non-MS and MS samples were not different (D). Nuclear staining with Bis-benzamide (blue) suggests no loss in cell number. Human tissue was obtained from the Rocky Mountain MS Center tissue bank. Data and figure from Thummala, 2015.

Since inflammation is another other major pathology in MS, we hypothesized that inflammatory-dependent axonal pathology causes the breakdown of the initial segment in MS. This is supported by previous work indicating a dual pathology in MS with demyelination and inflammation (Leray et al., 2010). The demyelination could lead to a loss of nodal clustering, while inflammation could lead to a loss of initial segments. To examine the effects of inflammation at the AIS, we used the inflammatory model of MS called Experimental Autoimmune Encephalomyelitis (EAE) as well as the inflammatory molecule Lipopolysaccharide (LPS) to induce inflammation.

Experimental autoimmune encephalomyelitis

EAE is a common animal model for MS. Like MS, it is a T-cell mediated disease characterized by inflammation and demyelination of the CNS (Gold et al., 2006; Kipp et al., 2009; Kipp et al., 2012). In EAE, a myelin antigen is injected along with Freund's complete adjuvant (mineral oil + heat killed *m. Tuberculosis*), and pertussis toxin, though specific protocols differ (Clark et al., 2016; Dupree et al., 2015; Gold et al., 2006). This cocktail stimulates an inflammatory immune response by macrophages, microglia, and T-cells against the CNS (Gold et al., 2006; Nicholson et al., 2009). EAE is unlike MS in that the specific antigens that can be used to induce it are known (Constantinescu et al., 2011; Huang et al., 2014; Huber et al., 2013). Proteolipid protein, myelin basic protein, and myelin oligodendrocyte glycoprotein (MOG) are common CNS antigens used to induce EAE (Kipp et al., 2012; Ramanathan et al., 2016; Recks et al., 2015; Terry et al., 2016). However, the presence of a CNS antigen is not directly required to induce EAE. Since it is a T-cell mediated disease, EAE can be stimulated in a healthy animal through transfer of T-cells from an EAE animal in a process known as "adoptive transfer" (Kipp et al., 2012; Zamvil et al., 1985). Regardless of the antigen or

technique used, the purpose is to stimulate an immune response against the CNS that resembles MS. The other components of the mixture used to induce EAE serve to stimulate toll-like receptors (TLR) on T-cells, priming them for an inflammatory immune response (Freund's complete adjuvant), and also disrupting the blood brain barrier and further inflaming the immune system (pertussis toxin) (Kipp et al., 2012; Richard et al., 2011).

For the current study, a segment of the MOG protein (amino acids 35-55) found on the N-terminal extracellular domain was used as the CNS antigen due to its effectiveness in stimulating a chronic encephalitic response in the CNS of C57/B16 mice (Ramanathan et al., 2016; Terry et al., 2016). MOG exists in the CNS on the outer myelin layer and on the surface of mature oligodendrocytes, making it an accessible antigen (Gold et al., 2006; Ramanathan et al., 2016). Antibodies to MOG have been shown to modify CNS inflammation, and T-cells can cross the blood brain barrier, further exacerbating the disease (Ramanathan et al., 2016). The inflammation in EAE (and MS) is associated with elevated levels of the inflammatory molecules tumor necrosis factor alpha (TNF α) and inducible nitric oxide synthase (iNOS) (Ummenthum et al., 2016; Valentin-Torres et al., 2016)

Lipopolysaccharide induced inflammation

As discussed previously, inflammation is a major insult in MS (Leray et al., 2010) and the inflammatory model EAE (Gold et al., 2006; Kipp et al., 2012; Varatharaj and Galea, 2016). Another molecule known to instigate an inflammatory response is lipopolysaccharide (LPS). LPS is an endotoxin found on the membrane of gram-negative bacteria that, like Freund's complete adjuvant in EAE, stimulates toll like receptors (TLRs) to induce an inflammatory response (Christmas, 2010; Heneka et al., 2000; Hoshino et al., 1999; Li et al., 2016; Qin et al., 2007). Similarly to EAE, peripheral LPS administration leads to the production of inflammatory

compounds such as $\text{TNF}\alpha$ and iNOS, and leads to neuronal damage as well as causing microglia, the immune cells of the CNS, to adopt a reactive morphology known as M1 activation (Fukushima et al., 2015; Hoshino et al., 1999; Liu and Bing, 2011; Qin et al., 2007; Taetzsch et al., 2015; Varatharaj and Galea, 2016). LPS induced inflammation is similar to the inflammatory aspects of EAE, while also being independent of peripheral immune cell infiltration. After a single peripheral administration of LPS (5mg/kg), we do not observe T-cell infiltration (Benusa and Dupree, unpublished observations). This makes LPS induced inflammation a valuable model to further investigate the effects of inflammation at the AIS.

Microglia: Immune Cells of the CNS

Microglia are considered the macrophages and resident immune cells of the CNS (Hanisch and Kettenmann, 2007). In the CNS, microglia exist along a spectrum of activation states. In the surveying state, microglia maintain a stationary cell body and are actively surveying the surrounding brain environment with processes extending to sample the environment at an average rate of $\sim 1.5\mu\text{m}/\text{minute}$ (Blaylock, 2013; Hanisch and Kettenmann, 2007; Nimmerjahn et al., 2005). Upon detection of a pathogen, signal or distress, microglia shift their level of activation by adopting an ameboid form and initiating transcriptional changes that make them actively phagocytic and pro-inflammatory. Activation of microglia broadly corresponds to macrophage activation, and can be termed M1 activated (classical activation, proinflammatory), or M2 activated (alternative activation, a complex state, but sometimes associated with healing) (Blaylock, 2013; Boche et al., 2013; Kettenmann et al., 2013; Taetzsch et al., 2015). M1 activated microglia secrete the pro-inflammatory molecule $\text{TNF}\alpha$, as well as increasing production of iNOS. iNOS is an enzyme that creates nitric oxide, a nitrogen radical and cell signaling molecule that can combine with oxygen radicals to create a destructive peroxynitrite

radical, further contributing to an inflammatory environment associated with neuronal damage (Blaylock, 2013; Ghasemi and Fatemi, 2014; Valentin-Torres et al., 2016). Microglia can both respond to and create inflammation, and while these cells are vital to the health and proper function of the brain, persistent M1 activation is associated with CNS damage in neurodegenerative diseases (Blaylock, 2013; Ghasemi and Fatemi, 2014; Hanisch and Kettenmann, 2007; Taetzsch et al., 2015; Valentin-Torres et al., 2016). Microglia were investigated in this study as possible mediators of AIS pathology.

Didox

Based on the hypothesis that inflammation is a major cause for damage to the initial segment, we treated animals with an anti-inflammatory drug called 3,4-dihydroxybenzohydroxamic acid, *Didox* (Molecules for Health Inc., Richmond, VA). *Didox* is a multifunctional drug that is a potent ribonucleotide reductase inhibitor and anti-inflammatory (Inayat et al., 2010; Matsebalela et al., 2015; Shah et al., 2015). The enzyme ribonucleotide reductase controls the rate limiting step in DNA synthesis, and inhibiting this enzyme is likely to affect rapidly dividing cells, such as those in tumors (Shah et al., 2015). *Didox* has been used for treating cancer (Shah et al., 2015) and it is also effective against inappropriate immune responses, such as those seen in graft versus host disease (Inayat et al., 2010). In a study examining allogeneic (antigenically foreign transplant tissue) inflammatory responses, Inayat et al. (2010) investigated the effects of *Didox* treatment on T-cells stimulated with anti-CD3- ϵ antibodies. Treatment with this antibody normally causes T-cells to proliferate and produce inflammatory cytokines, but they found that *Didox* blocked proliferation in the presence of anti-CD3- ϵ without significant cell death. It also blocked the production of interferon- γ (IFN-

γ), interleukin (Il)-4, and Il-6; which are all factors normally produced by inflamed T-cells (Inayat et al., 2010).

Macrophages have also been shown to be involved in inflammation through production of inflammatory cytokines and chemokines, reactive oxygen species, and phagocytosis (Matsebatlela et al., 2015; Wu et al., 2016). In order to determine the effectiveness of Didox in suppressing macrophage-mediated inflammation, Matsebatlela et al. (2015) used quantitative reverse transcriptase polymerase chain reaction (qRT-PCR) and other assays to examine the expression of murine macrophages under three conditions: LPS treatment, Didox treatment, and LPS + Didox. Didox significantly reduced the expression of inflammatory cytokines (TNF α , Il-6, Il-10) and inflammation-associated enzymes (iNOS, COX-2) normally produced in response to LPS (Matsebatlela et al., 2015). Didox also prevented the translocation of nuclear factor kappa B (NF κ B) to the nucleus, which could account for the suppressed inflammatory response in Didox treated macrophages (Matsebatlela et al., 2015). Due to the anti-inflammatory properties and results from previous studies, Didox was used for treatment of EAE and LPS-induced inflammation in this study.

Hypothesis

Our laboratory has previously shown that initial segments shorten in Early EAE, and significantly decline in number at the Late EAE time point (Clark et al., 2016) We proposed that attenuation of CNS inflammation might dampen the inflammatory-induced pathology. To test this hypothesis, mice were treated at Early EAE with the anti-inflammatory drug Didox. When treated at the early phase with Didox, the initial segments do not decrease in number at the Late EAE time point. This was a striking finding, as other studies indicated that the loss of initial segments was a permanent event (Schafer et al., 2009; Szu-Yu Ho and Rasband, 2011). If anti-

inflammatory treatment was ameliorating the degeneration of initial segments, could it also lead to the recovery of lost initial segments? This question led to my hypothesis: resolution of inflammation will rescue AIS disruption. We set about addressing this question using Didox to reduce inflammation in the previously described inflammatory disease models, EAE and LPS-mediated inflammation.

CHAPTER 2: Materials and Methods

Animals

Female C57BL/6 mice were obtained at 11 weeks of age from Jackson Laboratories (Bar Harbor, ME) and maintained in the Hunter Holmes McGuire Veterans Affairs Medical Center vivarium for the duration of the study. Upon arrival, all mice were allowed to acclimate for 1 week prior to induction. The mice were housed in groups of 4 in ventilated cages; food and water was available *ad libitum*.

The EAE study includes data from 3 cohorts of mice. Immunocytochemistry was performed on cohorts 1 and 2 (n=24 total), while cohort 3 (n=9 total) was used for western blot analysis and qRT-PCR. The LPS study includes mice from 1 cohort (n=22 total), which were all used for immunocytochemistry. Mice in all cohorts were maintained under the conditions as described above.

EAE Induction

In order to model the inflammatory aspects of Multiple Sclerosis, we induced EAE as described in Clark et al. (2016). Twelve week old mice received a subcutaneous injection between the shoulders of a cocktail consisting of an equal volume of MOG (6 mg/ml peptide in PBS, amino acid 35-55) (AnaSpec, Inc., Fremont, CA) and Freund's complete adjuvant (heat killed *M. tuberculosis* dissolved in mineral oil; 10 mg/ml *M. tuberculosis* in Freund's adjuvant)(Invitrogen Life Technologies, Grand Island, NY). Final concentrations are 3mg/ml MOG and 5 mg/ml complete Freund's adjuvant (*M. tuberculosis*/Freund's adjuvant). Mice also received an intraperitoneal (i.p.) injection of Pertussis toxin (300ng in 200ul of PBS/ mouse) (List Biological Labs, Campbell, CA). Mice received this pertussis toxin injection again 48 hours

later. Symptoms were scored based on a clinical score ranging from 0-5 as follows: 0 = no symptoms; 1 = limp tail, 2 = loss of righting reflex, 3 = single hind limb paralysis, 4 = both hind limbs were paralyzed, and 5 = death (Table 1).

Clinical Score	Symptoms
0	None
1	Limp tail
2	Limp Tail with loss of righting reflex.
3	Paralysis of single hind limb.
4	Paralysis of both hind limbs.
5	Death.

Table 1. Clinical scoring criteria. Animals were evaluated daily and assigned clinical scores based on symptoms to track the severity of EAE.

Clinical symptoms were first observed approximately 7-10 days post injection with a progressive disease course that typically peaked by 12-14 days post injection (Figure 3). Only mice that reached and maintained a clinical score of 3 and 4 were used in this study. Although typical disease course results in mice reaching and maintaining clinical scores of 3 and 4, the disease is highly variable. Not all mice developed symptoms or maintained clinical scores of 3 or 4. Mice were weighted daily and mice that lost >20% of their body weight were euthanized.

This study focused on mice at two time points, *Late EAE* and *Chronic EAE*. Late EAE is defined as 9 days past peak clinical score (a clinical score of 3 or 4 is defined as peak) and Chronic EAE is 9 days past Late EAE. Mice were treated with Didox for 8 days. Treatment was initiated the day following Late EAE, continued for 8 days, and mice were taken for analysis at the Chronic EAE time point (the morning following day 8 of treatment). Chronic EAE mice that received treatment with Didox will be known as “Didox”, and the untreated mice will be referred to as “Chronic EAE”. Only mice that maintained a peak score for 9 days (Late EAE) were included in the study (Figure 3, Table 2)

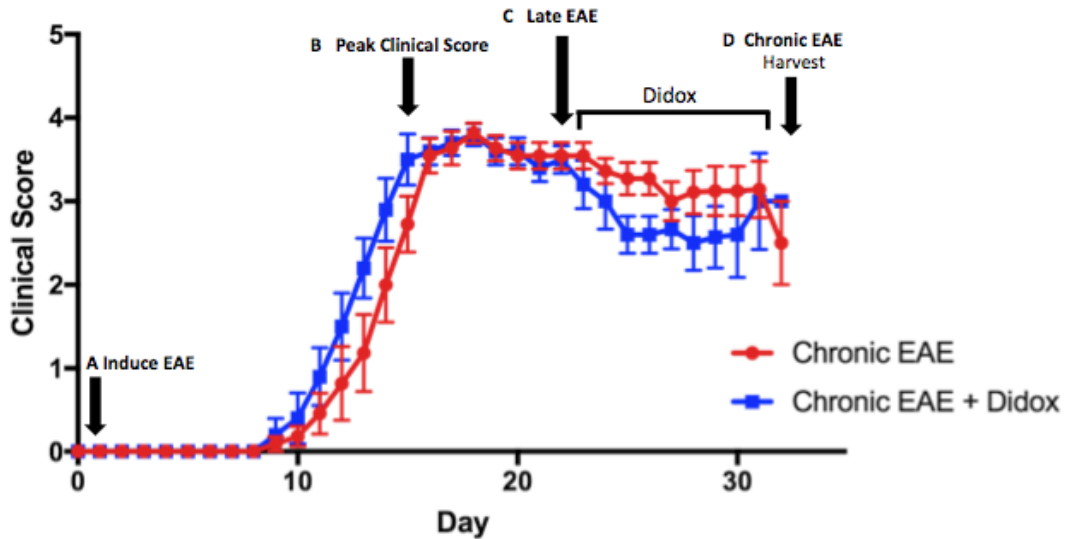


Figure 3. EAE experimental design. EAE is induced (A) and animals typically take ~10 days to start displaying clinical symptoms. Animals progress to peak clinical score (B), defined as a 3 or 4, within a week of displaying clinical symptoms. Animals must maintain a clinical score of 3 or 4 for 9 days to reach the Late EAE time point (C). Animals are divided into untreated (Chronic EAE) or treated with Didox for 8 days (Didox). Animals were harvested at the Chronic EAE time point (D). Note: all time points are defined by peak clinical score (C), which varies with every animal. Relative time points are represented on this graph.

Exclusion Criteria:

- **Mouse did not develop a clinical score.**
- **Mouse developed a clinical score, but recovered (returned to a score below a 3 or 4) at any time before reaching *Late EAE*.**

Table 2. EAE exclusion criteria. Only mice that reached the Late EAE time point were included in this study. Mice had to develop and maintain a clinical score of 3 or 4 for a period of 9 days in order to be included in the study.

Chronic EAE Didox Treatment

A cocktail of carboxymethylcellulose (0.5% w/v), sodium chloride (0.9%), polysorbate (0.4% w/v), and benzyl alcohol (0.9% w/v), all dissolved in deionized water, was used as the vehicle for Didox delivery and vehicle control. This cocktail is referred to as carboxymethylcellulose (Carboxy). In the EAE studies, Didox was administered at a dose of 550mg/kg in 200 μ l of carboxymethylcellulose. Didox was administered daily via oral gavage, beginning at Late EAE and continuing for 8 days.

The dosage, route of administration, and choice of vehicle have been previously established (Clark et al., 2016).

LPS-mediated Inflammation

LPS-mediated inflammation was also used to model aspects of CNS inflammation. Based on previous results from our lab, time points were defined to be analogous to those used in the Chronic EAE study and included 1 week post-LPS (1 Week LPS) and 2 weeks post-LPS (2 Week LPS). At the 1 Week LPS time point, saline control and 1 Week LPS mice were taken for analysis. The remaining mice were divided into groups to receive Didox (Treatment, Didox was dissolved in saline) or saline (vehicle control) treatment beginning the day following the 1 Week time point. Treatment continued daily for 8 days and mice were harvested at the 2 Week LPS & Didox time point 16 days post-injection (Figure 4).

LPS induced Inflammation Experimental Design

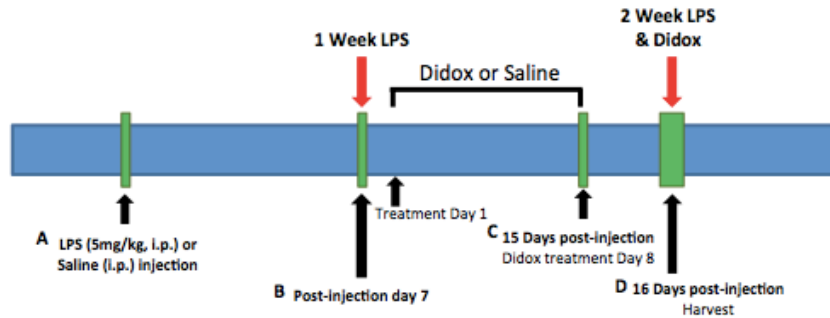


Figure 4. LPS experimental design. Based on previous results from our lab, time points were defined to study a prolonged model of LPS-induced inflammation. Mice received a single injection of LPS (5mg/kg) or saline (A). 1 Week post-injection, saline control and 1 Week LPS mice were taken for analysis (B). The remaining mice were divided into groups to receive Didox or vehicle control saline treatment beginning the morning following the 1 Week time point. Similarly to the EAE studies, treatment continued for 8 days (D). Didox (treated) and 2 Week LPS (vehicle control) mice were harvested 16 days post-injection for analysis.

16 mice received a single i.p. injection of LPS (Millipore, Billerica, MA) dissolved in saline at a dose of 5mg/kg, and 6 mice received a saline injection alone (control). Mice were monitored every 3 hours for the first 12 hours and then every 12 hours until 48 hours after injection. LPS injected mice exhibit a variety of symptoms including hunched posture, lethargy, head pressing, weight loss (not more than 20%) and dehydration. Mice were given 300 μ l of sterile 0.9% saline subcutaneously to maintain hydration and transgel (Bioserve Biotechnologies, Beltsville, MD) was made available ad libitum. Mice were euthanized if weight loss exceeded 20%.

LPS Study Didox Treatment

2 Week LPS + Didox (treatment, referred to as: Didox) mice received i.p. injections of Didox (Molecules For Health Inc., Richmond, VA) at a dose of 250mg/kg dissolved in 200 μ l of 0.9% saline daily for 8 days and were taken for analysis on the 9th day. 2 Week LPS + Saline (vehicle control, referred to as: 2 Week LPS) vehicle control mice received 200 μ l of saline for an equivalent period of time. Control mice received saline injections at the beginning of the study and were taken for analysis at the 1 Week time point.

Immunocytochemistry

Tissue Preparation

Treatment was continued for 8 days past the peak clinical score. On the morning of the 9th day, mice were deeply anesthetized using a solution of 2.5% avertin (2,2,2-tribromoethanol)(Sigma-Aldrich, St. Louis, MO). The avertin was in solution with 0.9% saline (Sigma-Aldrich) and administered at a dose of 0.016 mL/g of body weight. Mice were then transcardially perfused for 10 minutes with 4% paraformaldehyde (Ted Pella, Redding, CA), as described in Clark et al. 2016. Following perfusion, the brain was removed and placed in a solution of 30% sucrose in

Phosphate Buffered Saline (PBS) (137mM NaCl, 10mM Na₂HPO₄, 1.8mM KH₂PO₄, 2.7mM KCl; this solution will be referred to as *1X PBS*) for 48 hours to cryopreserve the tissue prior to freezing. The cerebellum was removed with a razor blade and discarded. The brain was then placed in optimal cutting temperature (OCT)(Tissue-Tek, Sakura Finetek USA, Inc., Torrance, CA) media and transferred to a -80°C freezer for preservation. After at least 4 hours in the freezer, the samples were sectioned on a Leica CM 1850 cryostat (Leica Biosystems, Buffalo Grove, IL). Sections were serially cut at a thickness of 40μm in the coronal plane. Sectioning began 2.5mm posterior to bregma and finished 1.1mm anterior to bregma. The sections were serially placed on 15 slides, starting with slice #1 on slide 1, then slice #2 on slide 2, and continuing for 15 slides. Slice #16 was placed in position two on slide 1, and so on until there were 6 sections per slide. Using this method, a single slide comprised a sample of ~3.0mm of cortex, with each section being ~600μm from each neighbor on a slide. All sections were stored at -80°C until they were used for immunolabeling.

Immunocytochemistry protocol

Slides were immunolabeled with antibodies directed against Ankyrin-G (AnkG)(NeuroMab, Davis, CA), βIV spectrin (kindly provided by Dr. Matthew Rasband, Baylor College of Medicine, Houston, TX), and Ionized calcium binding adapter molecule-1 (IBA-1) (Wako Chemicals; Richmond, VA).

First, the slides were selected and defrosted on the lab bench. Excess OCT was removed with a razor blade and a hydrophobic barrier was drawn around the perimeter of the slides with a PAP pen (Sigma-Aldrich, St. Louis MO). The slides were then placed in cold acetone for 10 minutes at -20°C in order to permeabilize the tissue. After this initial acetone wash, the slides were washed three times for 5 minute each in 1X PBS. After the final wash, the hydrophobic

barriers were blotted dry and a blocking and permeabilizing solution composed of 1X PBS, 0.5% Triton X-100 (MP Biomedicals, Solon, OH), and cold-water fish gelatin (Electron Microscopy Services, Hatfield, PA) was pipetted onto the slides. The slides then sat in a sealed, opaque box for 15 minutes at room temperature. After this initial block slides were tilted and a pipette was used to remove the blocking solution. Then the hydrophobic barrier was blotted to remove residual liquid and the primary antibody solution was added. The following primary antibodies were used:

Ankyrin-G

Axon initial segments were visualized using Ankyrin-G mouse monoclonal IgG_{2a} antibodies from NeuroMab (Davis, CA, clone N106/36). This antibody was generated against a synthetic peptide of 1000 amino acids from the Ankyrin-G protein. Detailed information on the location of this sequence within the Ankyrin-G molecule was not provided by the manufacturer. Using the National Library of Medicine's Basic Local Alignment Search Tool (BLAST), I compared the polypeptide sequence used to generate the monoclonal antibody to the full Ankyrin-G polypeptide sequence. BLAST analysis showed that the monoclonal antibody sequence is 98% identical to amino acid 873-1477 of AnkG (<http://blast.ncbi.nlm.nih.gov/Blast.cgi>). This stretch of amino acids encompasses the unique intracellular spectrin binding domain of Ankyrin-G (Kizatail, 2006). The Ankyrin-G antibody was used in a concentration of 1:200 diluted in the previously described blocking solution.

IBA-1

Microglia were visualized for qualitative analysis with a rabbit polyclonal IgG antibody generated against ionized calcium binding adaptor molecule 1 (IBA-1)(Wako Chemicals USA, Richmond VA). IBA-1 was used in a concentration of 1:1000. This polyclonal antibody is

generated against the C-terminal domain of IBA-1 and is commonly used to visualize the morphology of microglia (Clark et al 2016, Elmore 2015, Davalos 2012).

NeuN

A mouse monoclonal antibody against the neuronal nuclear protein (NeuN)(Millipore, Billerica, MA) was used to compare neuron nuclei number between treatment groups. NeuN was used at a concentration of 1:500. NeuN marks most neuronal nuclei, excluding cerebellar purkinje cells, olfactory bulb mitral cells, and retinal photoreceptor cells (Mullen et al., 1992).

Secondary Antibodies

After the primary antibody(ies) were added to the slides, the slides were placed back in the sealed box in a 4 °C refrigerator overnight. The following day, slides were quickly placed in 1X PBS to remove the primary antibody solution, and then washed three times in 1X PBS and blocked as previously described. After this block, the appropriate fluorescently labeled secondary antibodies were added and the slides incubated at room temperature in this solution for 90 minutes. An “appropriate” secondary antibody is one that is generated against the host species of the primary antibody. For example, since the monoclonal AnkG antibodies were generated in a mouse and were isotype IgG_{2A}, the secondary antibody used to label the primary antibody was generated in a goat *against* mouse IgG_{2a}.

All fluorescently labeled antibodies were purchased from Thermo Fisher Scientific (formerly: Life Technologies; Waltham, MA) and were used at a concentration of 1:500. After the secondary incubation, the slides were drained and the nuclear marker bis-Benzimide (Sigma-Aldrich, St. Louis MO) was added to the slides at a concentration of 1:1000 (diluted in 1X PBS) for 2 minutes. The slides were again washed three times for 5 minutes in 1X PBS and

coverslipped using the anti-fade reagent Vectashield™ (Vector Laboratories, Burlingame, CA), and placed in a slide box at 4°C until imaging.

Microscopy and Image Quantification

Chronic EAE

All images were collected using a Zeiss LSM 710 confocal laser scanning microscope (Carl Zeiss Microscopy LLC, Thornwood, NY), located in the Virginia Commonwealth University (VCU) Department of Anatomy and Neurobiology Microscopy Facility. Images for Ankyrin-G, and IBA-1 quantitation were taken from layer V of the neocortex as confocal z-stacks. Each image was 215 μ m tall, 215 μ m wide, and spanned an optical depth of 25 μ m. These dimensions define a field of view (FOV). Images were taken with a 40X oil immersion objective with a numerical aperture of 1.3, an optical slice thickness of 1.0 μ m and a scan average of 2; and 1 Airy unit. Gain, offset, and laser power were kept constant for all images (Table 3, A).

Ankyrin-G quantitation

Four images were collected from each of the six sections on a slide. Two images from cortical layer V of the left hemisphere, and two from cortical layer V of the right hemisphere, giving a total of 24 images per mouse. Neocortical layer V was identified based on the sparse nuclei distribution (visualized through bis-benzamide nuclear staining) of layer V when compared to the more tightly packed nuclei of layer IV and layer VI. Ankyrin-G was quantified manually as described below.

NeuN quantitation

NeuN staining was visualized for Neuron viability. A sample of 3 mice were taken from each treatment group (3 Naïve, 3 Late EAE, 3 Chronic EAE, and 3 Didox) for NeuN quantification. A

single optical slice was taken from layer V of each hemisphere on slice 2 from each slide (2 images per slide). This yielded approximately 250+ cells per image or 500+ cells per slide. Microscope settings were kept constant for EAE NeuN quantitation (Table 3, B). These images were processed and quantified using the automated counting method described in Chapter 6 to count the cells per image.

A Microscope Settings for Chronic EAE initial segment and microglia quantitation.

Master Gain	Ch1: 662 Ch2: 674
Offset	0
Pinhole Diameter	34µm, 1 airy unit
Zoom	1
Objective	40X oil immersion
Line Averaging	2
Step size	1.0µm
Bit	16 bit
Image dimensions	x:215.04µm; y: 215.04µm; z: 25µm
Dimensions	x: 2288; y: 2288; z:26
Lasers	561nm: 11.4% 488nm: 8.0%
Scan Mode	Step

B Microscope settings for Chronic EAE Nuclei quantitation.

Master Gain	Ch1: 582 Ch2: 675
Offset	0
Pinhole Diameter	31µm
Zoom	1
Objective	20X/0.8 M27 Plan Aplanachromat
Line Averaging	4
Step size	NA
Bit	16 bit
Image dimensions	x:424.94µm; y: 424.94µm
Dimensions	x: 2780; y: 2780; 2 channels
Lasers	561nm: 7.5% 488nm: 24.0%
Scan Mode	Plane

Table 3. Zeiss LSM 710 microscope settings for the Chronic EAE study. Ankyrin-G, IBA-1, and NeuN were collected using consistent settings on the Zeiss 710 Laser Scanning Confocal Microscope. All images were collected at the VCU Microscopy Facility.

LPS-mediated Inflammation

For the LPS study, an identical procedure was used, except one image was taken from each hemisphere on each slice, yielding 12 images per mouse. Microscopy settings were kept constant for all quantitated images in LPS-mediated inflammation (Table 4, A).

NeuN quantification

NeuN staining was visualized for Neuron viability. A sample of 3 mice were taken from each treatment group (3 Controls, 3-1 Week LPS, 3-2 Week LPS, and 3 Didox) for NeuN quantification. A single optical slice was taken from layer V of each hemisphere on slice 2 from each slide (2 images per slide). This yielded approximately 250+ cells per image or 500+ cells per slide. Microscope settings were kept constant for EAE NeuN quantitation (Table 4, B). These images were also processed and quantified in the same manner as NeuN quantitation for the Chronic EAE study.

A Microscope Settings for LPS-induced inflammation initial segment and microglia quantitation

Master Gain	Ch1: 762 Ch2: 695
Offset	0
Pinhole Diameter	34µm, 1 airy unit
Zoom	1
Objective	40X oil immersion
Line Averaging	2
Step size	0.436µm
Bit	16 bit
Image dimensions	x:215.04µm; y: 215.04µm; z: 24.88µm
Dimensions	x: 2288; y: 2288; z:26; 2 channels.
Lasers	561nm: 30.0% 488nm: 11.4%
Scan Mode	Step

B Microscope settings for LPS-induced inflammation Nuclei quantitation

Master Gain	ChS2: 513 Ch2: 629
Offset	0
Pinhole Diameter	36nm, 1 airy unit
Zoom	1
Objective	20X/0.8 M27 Plan Aplanachromat
Line Averaging	4
Step size	NA
Bit	16 bit
Image dimensions	x:424.04µm; y: 424.04µm
Dimensions	x: 2412; y: 2412; 2 channels.
Lasers	633nm: 40% 561nm: 40%
Scan Mode	Plane

Table 4. Zeiss LSM 710 microscope settings for LPS-mediated inflammation study. Ankyrin-G, IBA-1, and NeuN were collected using consistent settings on the Zeiss 710 Laser Scanning Confocal Microscope. All images were collected at the VCU Microscopy Facility.

Image Quantification

For the EAE study, the length and quantity of initial segments in each image, or field of view (FOV; a field of view consists of an area $215.04\mu\text{m} \times 215.04\mu\text{m} \times 25\mu\text{m}$), were determined using the manual tracing function on the ImageJ analysis software in a manner previously described in Clark et al. (2016). Maximum intensity projections were created in ImageJ from the optical stacks and the initial segments of each image were traced and measured. To eliminate the counting of AISs that extended beyond the boundaries of the FOV, any AIS touching one of the 6 edges of the optical stack was not traced or counted. Microsoft Paint (Microsoft, Redmond, Washington) was used to mark any AISs that appeared in the very first, or in the very last optical slice before they were compressed into a maximum intensity projection. Once the slices were compressed on ImageJ, a mark was visible on any initial segments that were not completely contained in the image stack. These initial segments were excluded from quantification. Ankyrin G labeling measuring less than $10\mu\text{m}$ in length were excluded from both counts and length measurements, as described in Schafer et al. (2009).

AIS counts and lengths were collected by FOV per mouse. For quantifying AIS number, the AISs per field of view were recorded, and an average was calculated per FOV for that mouse. This allowed an average number of AISs per FOV for each mouse in a treatment group to be calculated. Once these numbers were established for mice in a treatment group, the groups were compared based on % of Naïve \pm standard error of the mean (SEM).

AIS length was collected by measuring the manual traces on initial segments. The average length per FOV per mouse was calculated and mice were compared by treatment group. Results are presented as the average length in $\mu\text{m} \pm$ SEM.

Automated Quantitation

A method for automated quantitation of initial segments and neuronal nuclei was developed and used for the LPS-mediated inflammation portion of this study. For details of the automated procedure and an analysis of the automated technique compared to manual counting methods, see Chapter 6.

Western Blots

Tissue Processing

Western Blotting was performed as previously described (Pomicter et al., 2010). Mice were deeply anesthetized with Avertin; the brain was dissected and the cortex was removed, placed in centrifuge tubes, flash frozen in liquid nitrogen, and stored at -80°C. For homogenization, frozen neocortices were placed in RIPA buffer (1% nonidet P40, 0.5% Sodium deoxycholate, 0.1% sodium dodecyl sulfate, and 1X PBS)(Sigma-Aldrich, St. Louis, MO) containing protease inhibitor cocktail (PIC) (Sigma-Aldrich, St Louis, MO). RIPA buffer with PIC is used to cause cell lysis and minimize protein degradation. 2ml of RIPA buffer with PIC was added to each sample's conical tube and the samples were homogenized with a Glas-col motor driven homogenizer (Terre Haute, IN, USA) at a speed of 60 for 10 strokes (a stroke is defined as the pastel moving from the top of the Eppendorf tube to the bottom, then back to the top). After homogenization, the samples were centrifuged at 2911 revolutions per minute (RPM) for 10 minutes at 4°C. Supernatants were collected and transferred to labeled microcentrifuge tubes, which were stored at -20°C.

Protein Assay

Supernatant protein concentration was determined using the Micro BCA Protein Assay Kit (Thermo Scientific, Rockford, IL) in order to ensure equivalent protein loading for western

blot gel electrophoresis. From the manufacturer's protocol (Thermo Scientific Rockford IL; Thermo # 23235): Bovine serum albumin (BSA)(Thermo Scientific, Rockford, IL) was serially diluted with 1X PBS to create eight standards (labeled S1-S8, with concentrations 2mg/ml, 1.5mg/ml, 1mg/ml, 0.75mg/ml, 0.5mg/ml, 0.25mg/ml, 0.125mg/ml, and 0.025mg/ml respectively) and a "blank" that contained PBS without BSA. 25 μ l of each of the BSA standards and the blank were added to a 96 well plate in duplicate. 10 μ l of the tissue sample supernatant was then diluted in 100 μ l of 1X PBS, and added to the same 96 well plate in duplicate below the standards. The BCA assay kit reagents A, B, and C were mixed at a ratio of 25:24:1 and 200 μ l of the resulting solution was added to each of the occupied wells. The plate was then incubated at 37°C for 15 minutes and cooled before being read in a spectrophotometer. A standard curve was generated using the sample absorbance values and used to determine protein concentrations of the samples.

Western Blot Protocol:

Protein concentrations determined from the BSA Protein Assay were normalized by diluting with sample buffer (Laemmli Sample buffer, β -mercaptoethanol 20:1) to ensure a standard 20 μ g load of protein per lane. The diluted samples were then boiled for 5 minutes and immediately placed on ice. After cooling, they were briefly centrifuged for 2 minutes at 10,000 RPM, and 10 μ l of solution containing 20 μ g of protein was added to a in a precast Criterion™ TGX™ 10 well gel (4-15% polyacrylamide; Bio-Rad, Hercules, CA). 10 μ l of molecular weight marker (Bio-Rad, Hercules, CA; Precision Plus Protein™ Kaleidoscope™) was added to the first lane as a standard weight measurement. The Western blot apparatus (Bio-Rad Mini Protean Tetra cell; Bio-Rad, Hercules, CA) was filled with running buffer (100 mL of 10X Tris-Glycine (0.25M Tris; 1.92M Glycine (Thermo Fisher Scientific Waltham, MA), 1g of Sodium dodecyl

sulfate, and 900 mL of deionized water), and the gel was set to run at 70V for 30 minutes initially, then at 100V for an additional hour. The gels were then removed, placed in transfer buffer (10X Tris-Glycine, 20% Methanol (Thermo Fisher Scientific Waltham, MA)), and were rocked in this solution for 15 minutes. A nitrocellulose membrane was cut to fit the gel and rocked in a transfer buffer for 15 minutes as well. A transfer cassette was prepared by sandwiching the sample gel and nitrocellulose paper between 2 blotting papers and 2 sponges. This transfer cassette was then placed in a gel box under ice, and connected to a power supply at 100V for 2 hours. Following the transfer, the gel was discarded and the nitrocellulose paper was washed in PBST (1X PBS and 0.05% Tween (Thermo Fisher Scientific Waltham, MA)) and incubated with a blocking solution composed of 3% non-fat dry milk (Nestle, Switzerland) and PBST for 40 minutes. The membrane was incubated overnight in a primary antibody blocking solution at 4°C.

Rabbit polyclonal anti- β IV Spectrin was used to probe for the AIS cytoskeletal component β IV spectrin. This antibody was used at a concentration of 1:2000 and was generously provided by Dr. Matthew Rasband of Baylor College of Medicine.

A mouse monoclonal antibody against inducible nitric oxide synthase (iNOS)(BD Biosciences, San Jose, CA) was used at a concentration of 1:2000 to quantify protein expression of this inflammatory marker. iNOS is often elevated in MS, EAE, and LPS-induced inflammation (Valentin-Torres 2016, Hu 2016, Kipp 2016, Taetzsch 2015).

Mouse anti-GAPDH antibody (Millipore, Billerica, MA) was used at a concentration of 1:10,000 as a loading control for all western blot experiments.

Two methods were used for visualizing proteins on western blot experiments: chemiluminescence, and fluorescent secondary antibodies.

Chemiluminescence

The following day, the nitrocellulose membrane was washed in PBS 3 times, for 10 minutes each, blocked for 20 minutes, and incubated in a secondary antibody solution for 1.5 hours before imaging. Western blots were finished with horseradish peroxidase conjugated secondary antibodies (Santa Cruz Biotechnology, Santa Cruz, CA). These antibodies were Goat-anti-mouse for iNOS and GAPDH, and Goat-anti-Rabbit for β IV spectrin. The secondary antibodies were diluted 1:10,000 in blocking solution. StrepTactin-HRP (Santa Cruz Biotechnology, Santa Cruz, CA) was also added to the secondary antibody solution to visualize the ladder. Following a 1.5 hour incubation, enzyme chemiluminescence reagents (Millipore, Billerica, MA) reagents were combined in a 1:1 ratio and the blot was imaged in a Bio-Rad ChemiDoc Touch® imaging system (Bio-Rad, Hercules, CA).

Fluorescent Secondary Antibodies

The following day, the nitrocellulose membrane was washed in PBS 3 times for 10 minutes each wash, blocked for 20 minutes, and incubated in a secondary antibody solution for 1.5 hours. The secondary antibody solution was composed of IRDye® 800CW Goat anti-Rabbit and IRDye® 680RD Goat anti-Mouse. These fluorescent antibodies were both purchased from LI-COR (Lincoln NE) and used at a concentration of 1:15000. After the incubation, the nitrocellulose paper underwent two 5 minute washes in PBST followed by four 10 minute washes in PBS alone. The nitrocellulose blots were then read on a LI-COR Odyssey® Infrared Imaging System (Lincoln NE) for quantitative analysis.

Densitometry

Western blot bands were analyzed using ImageJ (NIH). Lanes were selected and band densities per lane were graphed by the *Analyze Gels* Plugin. The area under the curve (optical

density) was determined using the wand tool (Pomicter et al., 2010). This process was repeated and the values recorded for each protein of interest and each loading control. The optical density of each protein of interest was then divided by the optical density of the respective loading control (GAPDH) to yield a relative quantity.

Quantitative Reverse Transcriptase Polymerase Chain Reaction (qRT-PCR)

RNA extraction

Total RNA was extracted from mouse cortices using a trizol (Ambion Invitrogen, Thermo Fisher Scientific Waltham, MA) homogenization and extraction method described in Taetzsch 2014. Mice were deeply anesthetized with Avertin and perfused with 0.9% NaCl; the brain was dissected and the cortex was removed, placed in microcentrifuge tubes, flash frozen in liquid nitrogen, and stored at -80°C . Brain cortices were homogenized with a Glas-col motor driven homogenizer (Terre Haute, IN, USA) in 1mL of trizol. Samples were centrifuged at $12,000\times g$ for 10 minutes at 4°C . Supernatant was collected and samples sat at room temperature for 5 minutes. $200\mu\text{l}$ of chloroform (Thermo Fisher Scientific Waltham, MA) was added to the samples and mixed by inversion. Samples sat for 10 minutes at room temperature before being centrifuged at $12,000\times g$ for 15 minutes at 4°C . The aqueous phase was transferred to a new microcentrifuge tube and an equal amount of 100% isopropanol (VWR Chemicals, Randor, PA) was added. Samples were mixed by inversion and placed at room temperature for 10 minutes, and centrifuged at $12,000\times g$ for 15 minutes at 4°C . The supernatant was removed and the RNA pellet was washed twice with 75% ethanol (VWR Chemicals, Randor, PA) and homogenized. Samples were centrifuged at $7500\times g$ for 5 minutes at 4°C and the pellet was air dried for 10-15 minutes before being re-suspended in $100\mu\text{l}$ of DEPC water.

RNA Purification

RNA samples were purified using the Qiagen RNeasy kit (Qiagen, Venlo, Netherlands) according to manufacturer's instructions. Briefly, 350 μ l of Qiagen buffer RLT was added to 100 μ l of RNA and mixed by inversion. 250 μ l of 100% ethanol (VWR Chemicals, Randor, PA) was added to the RNA and this solution was mixed by pipetting. The samples were transferred to RNeasy spin column and placed in a 2ml collection tube. Samples were centrifuged for 15s at 8000xg. 500 μ l of buffer RPE was added to the RNeasy column and centrifuged at 8000xg for 2 minutes. After this centrifugation step, the spin column was transferred to a new collection tube and centrifuged at 16,000xg for 1 minute. RNA was eluted using 30 μ l of RNase free water and a 1 minute centrifugation at 8000xg.

DNase Treatment

First, RNA concentration and purity was measured using a nanophotometer and only samples with an absorbance ratio (260nm/280nm) >1.8 were included (Implen GmbH, Germany). An Ambion DNA Free Kit (Thermo Fisher Scientific Waltham, MA) was then used to remove contaminating DNA. 12 μ l of DNase was added to each sample and then samples were incubated for 30 minutes at 37°C. After this incubation, 10 μ l of DNase inactivation reagent was added to each sample. Samples were then incubated for 2 minutes at room temperature. Samples were centrifuged at 10,000xg for 1.5 minutes and the supernatant collected.

Reverse Transcription

iScript Reverse Transcription Supermix (BioRad, Hercules, CA) was used to create cDNA from sample RNA. Samples were prepared with 4 μ l of BioRad 5X iScript supermix followed by 16 μ l RNA sample in a 100 μ l Veriti Thermal Cycler tube (Thermo Fisher Scientific Waltham, MA) and mixed by repeated pipetting. A no reverse-transcriptase (RT) control was

prepared by adding 16 μ l of RNA from a sample (Late EAE sample) to 4 μ l of no- reverse transcriptase BioRad 5X iScript supermix. Samples and the no-RT control were spun down and placed in an Applied Biosystems Veriti Thermal Cycler (Thermo Fisher Scientific Waltham, MA) set to run for 5 minutes at 25°C, 30 minutes at 42.5°C, and 5 minutes at 85°C. Samples were then stored at -20°C.

qPCR

Primers were designed for iNOS, TNF α , and the housekeeping gene cyclophilin A (Cyclo A) using the National Center For Biotechnology Information (NCBI) website (**Error! Reference source not found.**). These primers were previously used in the lab (Clark et al., 2016). Samples were run with each primer in duplicate. A no-RT control and a no-template (no cDNA, containing just water) control was also run for each primer set. Master mixes were prepared for 19 μ l per well for the target and reference gene. 10 μ l of BioRad SsoFast Evagreen Supermix (BioRad, Hercules, CA) was combined with 0.5 μ l of the forward primer (primer concentration is 20 μ M), 0.5 μ l of the reverse primer, and 8 μ l of DNase free water. The master mix contains a final primer concentration of 500nM. Master mixes were prepared, mixed and spun down for target and control genes. Master mix was then added to the appropriate wells of a 96 well plate and 1 μ l/well of sample cDNA was added. The plate was sealed and run in a BioRad thermal cycler at the following cycling parameters: one cycle at 95°C for 5 minutes, 40 cycles of 95°C (5s) and 56°C (5s) followed by the generation of a melt curve through a series of 5 second 0.5°C incremental temperature increases from 65°C to 95°C.. The fold changes in the expression of target genes were calculated using the formula $RQ=2^{-\Delta\Delta C_t}$.

Gene	Primers
TNFα	Forward: 5'-GCCACGTCGTAGCAAACCACC-3'
	Reverse: 5'-CCCATCGGCTGGCACCCTA-3'
iNOS	Forward: 5'-TCCAGAATCCCTGGACAAGCTGC-3'
	Reverse: 5'-TGCAAGTGAAATCCGATGTGGCCT-3'
Cyclo A	Forward: 5'-CTAGAGGGCATGGATGTGGT-3'
	Reverse: 5'-TGACATCCTTCAGTGGCTTG-3'

Table 5. qRT-PCR primer sequences. TNF α , iNOS, and Cyclo A primers were designed using the NCBI website.

Statistical Analysis

To compare the number of initial segments, the data are presented as percent of naïve (% naïve \pm standard error of the mean (SEM)). To compare AIS length, the average length of the AISs (in μm) is presented as mean length \pm SEM. Mice were averaged and compared by treatment group with one-way analysis of variance (ANOVA) and Tukey's Honest Significant difference (HSD) post hoc test. When appropriate, t-tests were used to compare two groups independently. All graphing and statistical analyses were performed using GraphPad Prism version 6.03 for Windows or OSX (GraphPad Software, San Diego, CA, USA). For western blot experiments, an average was computed per treatment group and the values were compared using one-way ANOVA. qRT-PCR data was analyzed in the same manner.

Data was processed from the automated analysis technique using the R programming language (R Core Team, 2015) but statistics were performed using GraphPad Prism. Along with base R functions, the following packages were used for organizing and summarizing data: ggplot2 (Wickham, 2009), reshape2 (Wickham, 2007), and dplyr (Wickham and Francois, 2015).

Chapter 3: Chronic EAE Results

AIS numbers are reduced in Chronic EAE

To investigate the effect of prolonged inflammation on AIS stability, initial segments were analyzed in Naive, Late EAE, Chronic EAE, and Chronic EAE + Didox (Didox) animals. Initial segments were quantified by manual tracing in ImageJ for the EAE studies. In Late EAE mice there was an average loss of $37\pm 10.4\%$ of initial segments compared to naive controls, and mice at the Chronic EAE time point displayed an average loss of $43.5\pm 11.6\%$ of AISs. Mice treated with anti-inflammatory Didox displayed a loss of $21.9\pm 8.9\%$ of initial segments compared to naive controls. Although there appears to be a decrease in initial segment numbers at the Late and Chronic EAE time points and a recovery with Didox treatment, one-way ANOVA indicates that there is no significant difference among groups (Figure 5).

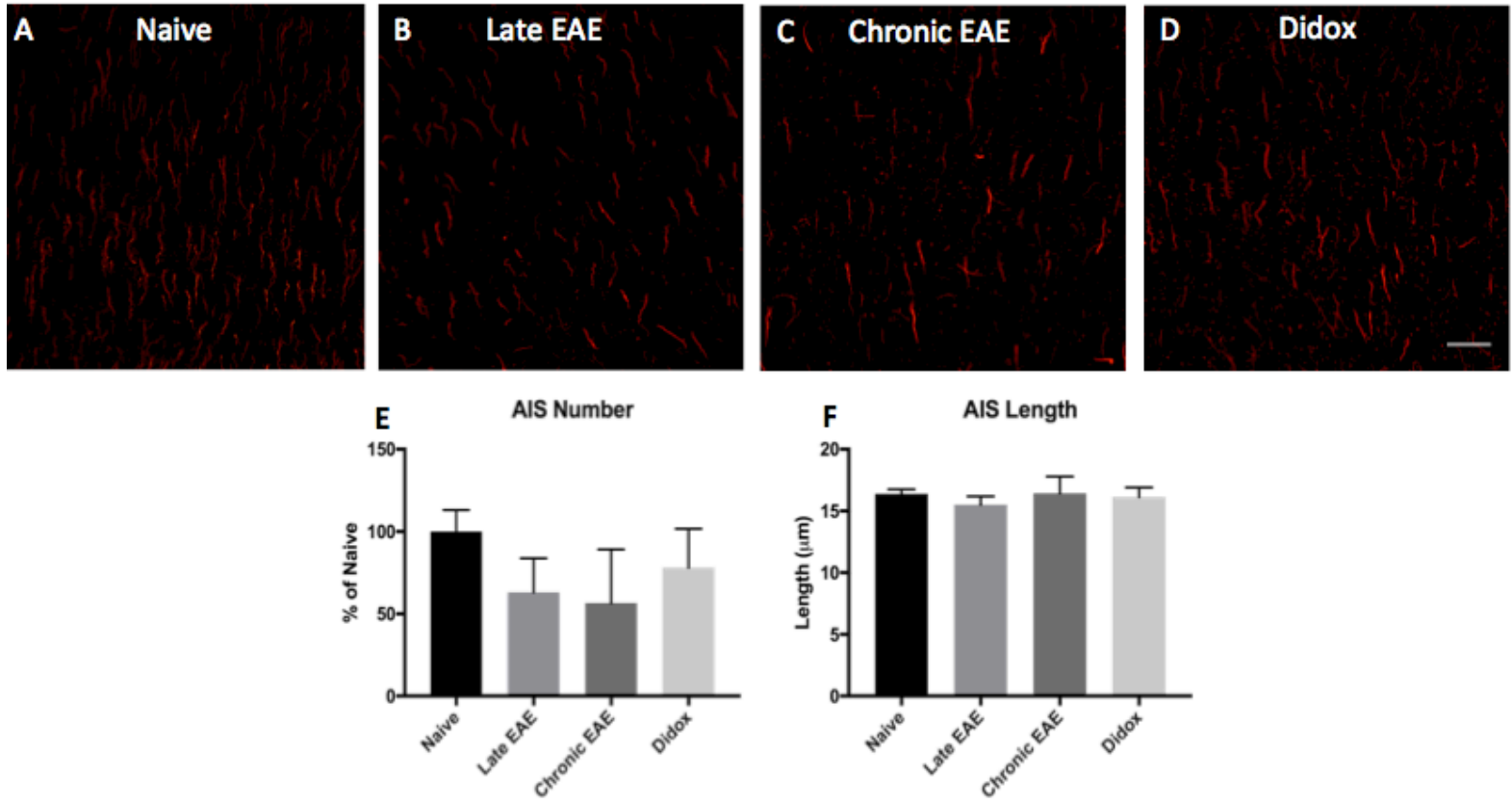


Figure 5 AIS number and length in Chronic EAE. The number of AISs are decreased by 37% at the Late EAE (B) time point compared to Naïve controls (A,E). There is a 43.5% decrease in AISs at the Chronic EAE (C,E) time point and a 21.9% loss following treatment with Didox (D,E). Despite these changes, results were not significant following one-way ANOVA. Average AIS length was unchanged during these time points (F) (n=4-8 at each time point, scale bar = 20μm).

AIS Length is not different in Late and Chronic EAE

In previous studies from our laboratory, we have reported a significant shortening of AISs at the early EAE time point, followed by a significant loss in AIS number at the late EAE time point. To determine if the significant shortening of the AISs was preserved in the chronic disease stage, we measured AIS length in Naive, Late EAE, Chronic EAE, and Didox mice. No significant difference in AIS length was detected. Naive mice displayed an average length of $16.4 \pm 0.2 \mu\text{m}$, Late EAE mice displayed an average of $15.5 \pm 0.3 \mu\text{m}$, Chronic EAE mice displayed an average of $16.5 \pm 0.5 \mu\text{m}$ and Didox mice displayed an average of $16.1 \pm 0.3 \mu\text{m}$ (Figure 5).

Neuron cell count is not changed in Late or Chronic EAE

In order to determine if the apparent reduction in AIS number was a consequence of neuron cell loss, sections were immunolabeled with NeuN, a marker of neuronal nuclei, and the numbers were quantitatively compared among the Naive mice and all treatment groups. An average NeuN+ cell count of 262.5 ± 8.8 NeuN+ cells (NeuN+)/FOV in Naive mice, 275.7 ± 11.8 NeuN+/FOV in Late EAE, 262.2 ± 16.3 NeuN+/FOV in Chronic EAE, and 275.3 ± 18.8 NeuN+/FOV in Didox was detected. There was no significant difference in neuronal counts between treatment groups (Figure 6).

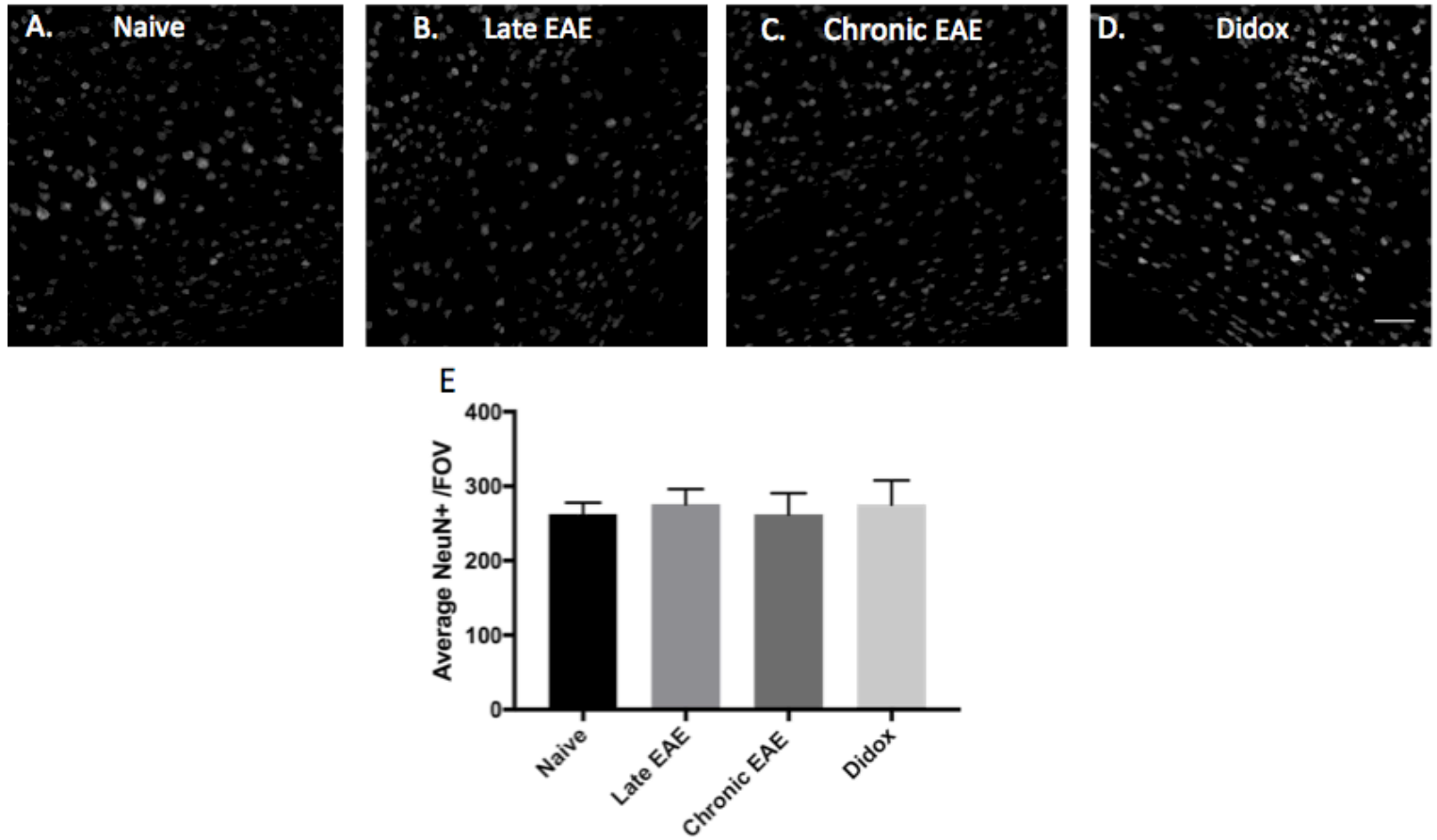


Figure 6. NeuN+ nuclei loss is not detected in Chronic EAE. NeuN was used to label neuronal nuclei in Naïve (A), Late EAE (B), Chronic EAE (C), and Didox (D) animals. Group means were compared using one-way ANOVA. No significant changes were detected (E) (n=3 mice at each time point, scale bar= 50 μ m).

Microglia display a less reactive morphology in Chronic EAE

In our previous work, we identified microglia, the resident immune cells of the CNS, as a candidate driver of AIS pathology. To begin to assess the inflammatory environment within the cortex, microglia were identified by IBA-1 immunolabeling and cell morphology was qualitatively compared among groups. Qualitative analysis of microglia morphology revealed that microglia are reactive in Late EAE, but show decreased reactivity in both Chronic EAE and Didox animals, as microglia with surveying phenotypes were readily observed in these mice (Figure 7). These observations are consistent with a reduced inflammatory environment in both Chronic EAE and Didox treated animals.

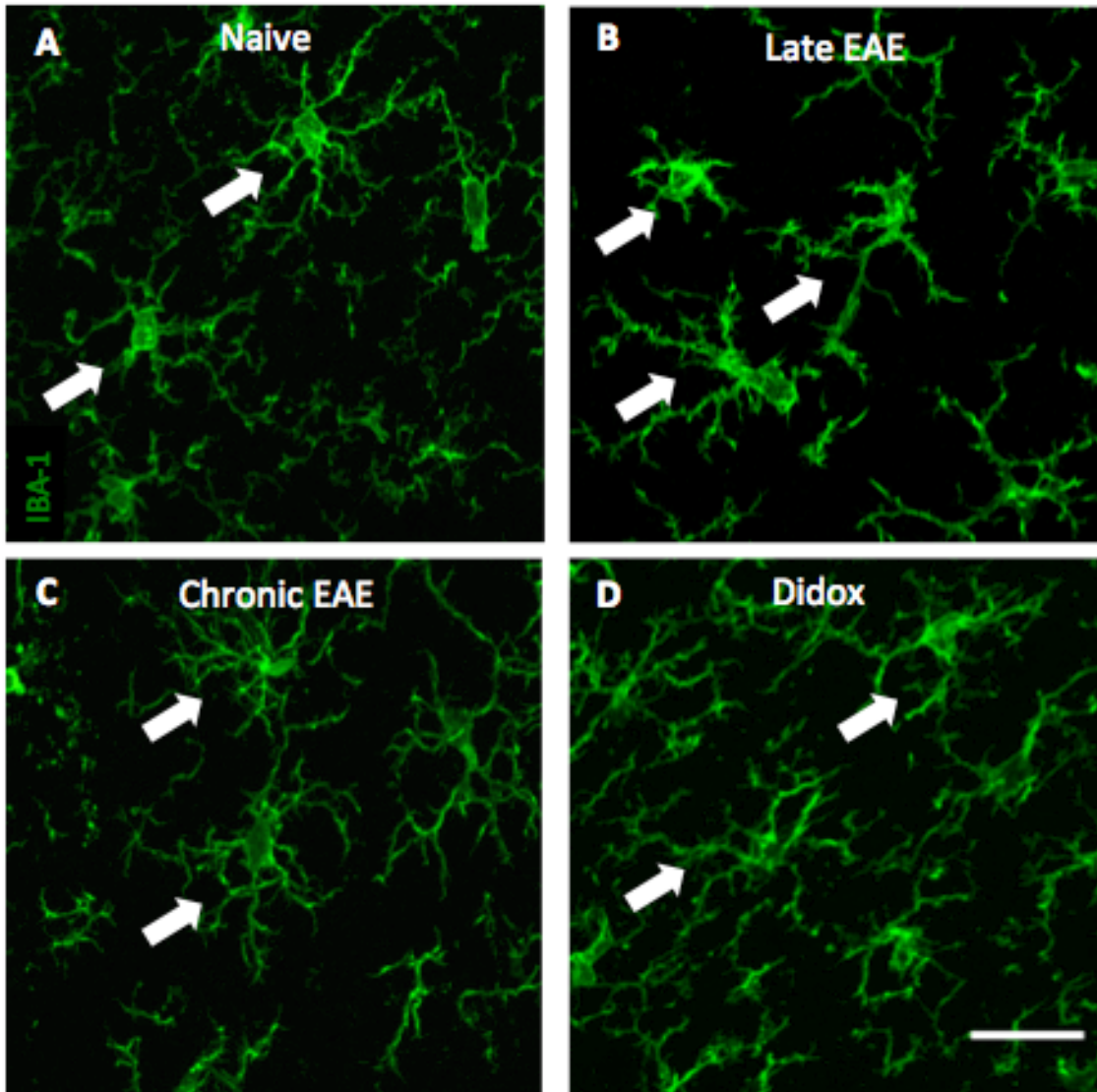


Figure 7. Microglia reactivity in Chronic EAE. Microglia display a ramified, surveying phenotype in Naïve mice (A). Microglia adopt a reactive morphology in Late EAE with larger cell bodies and shorter, thicker branches (B). Microglia reactivity decreases in both Chronic EAE and Didox mice (C and D)(scale bar= 20 μ m).

Inflammatory markers TNF α and iNOS are increased in the EAE Cortex

Although morphological changes of the microglia were consistent with increased inflammation in Late EAE mice and an apparent resolution in the microglial morphology indicating a reduced inflammatory environment in the Chronic EAE and Didox mice, morphology is not always a reliable indicator of microglia function (Hanisch and Kettenmann, 2007; Taetzsch et al., 2015). To further investigate the inflammatory environment within the cortex, qRT-PCR was used to assess the levels of two inflammatory markers, TNF α and iNOS. Target gene values were normalized to the housekeeping gene Cyclo A using the formula $RQ=2^{-\Delta\Delta Ct}$ to calculate fold changes in expression (Taylor 2010).

Expression levels of TNF α were significantly increased in the cortices of Chronic EAE animals compared to Naïve controls (average of 6.9 ± 1.1 in Chronic EAE and 0.6 ± 0.2 in Naïve animals). Treatment with the anti-inflammatory Didox significantly decreased TNF α expression at the Chronic EAE time point (2.4 ± 0.2 in Didox compared to 6.9 ± 1.1 in Chronic EAE). Didox levels were not significantly different from Naïve (2.4 ± 0.2 in Didox and 0.6 ± 0.2 in Naïve animals)(Figure 8).

iNOS expression was increased in Chronic EAE animals (average of 6 ± 2.8 for Chronic EAE versus an average 1.2 ± 0.2 for Naïve), and further decreased following treatment with Didox (average expression of iNOS with Didox treatment of 0.8 ± 0.2 compared to 1.2 ± 0.2 for Naïve). Although there was a 6-fold increase in average iNOS expression levels, the groups were not significantly different from one another (Figure 9).

Additionally, protein levels of the pro-inflammatory mediator iNOS were measured via western blot analysis and standardized based on the GAPDH loading control. Densitometry revealed no significant difference in immunoreactive iNOS bands between groups (Figure 10).

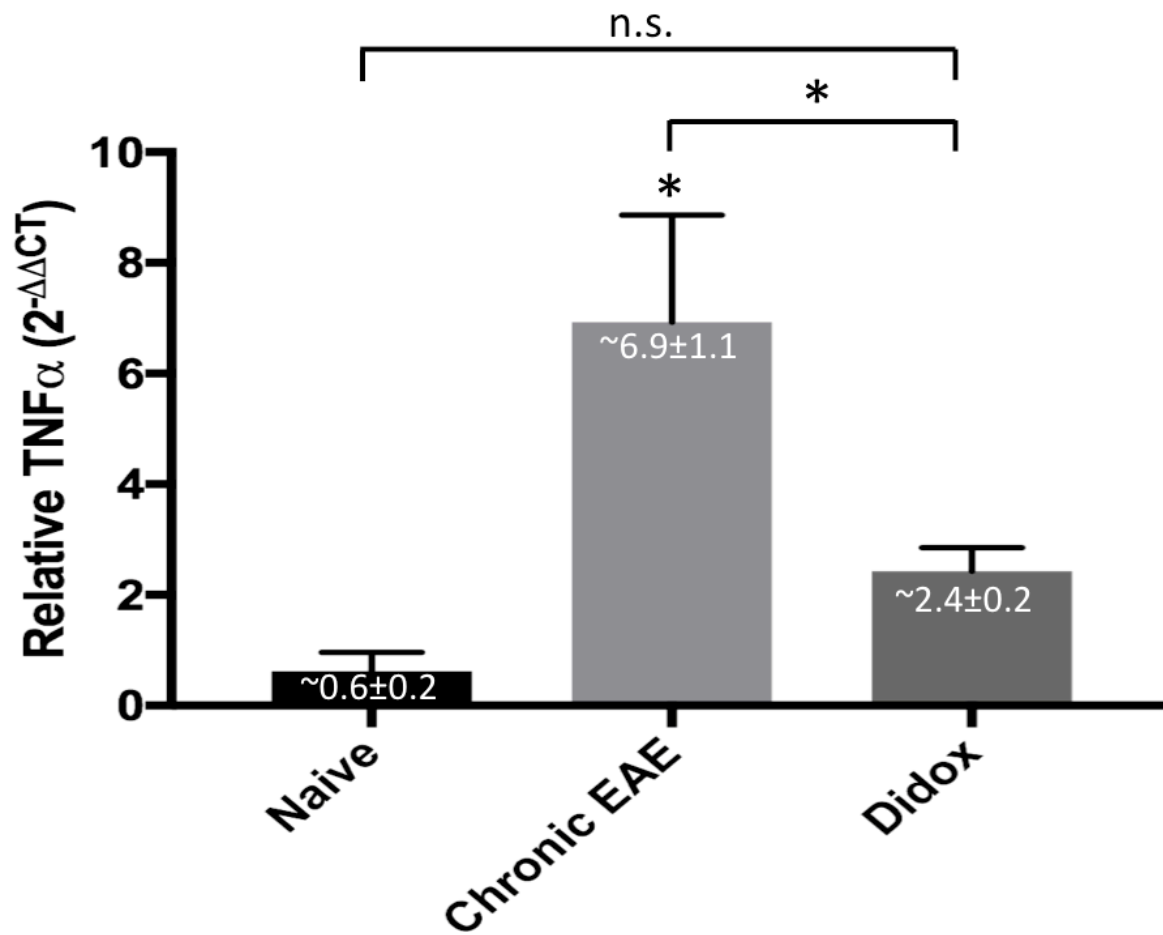


Figure 8. TNF α mRNA levels are significantly increased in the cortex of Chronic EAE mice. Cortical mRNA levels of TNF α in Chronic EAE mice were elevated 7 fold (6.9 ± 1.1) above levels measured in Naïve mice (0.62 ± 0.2). Didox treated animals displayed levels of TNF α that were not significantly different than Naïve (2.4 ± 0.2) (one-way ANOVA, $p < 0.01$, $n = 3$ at each time point).

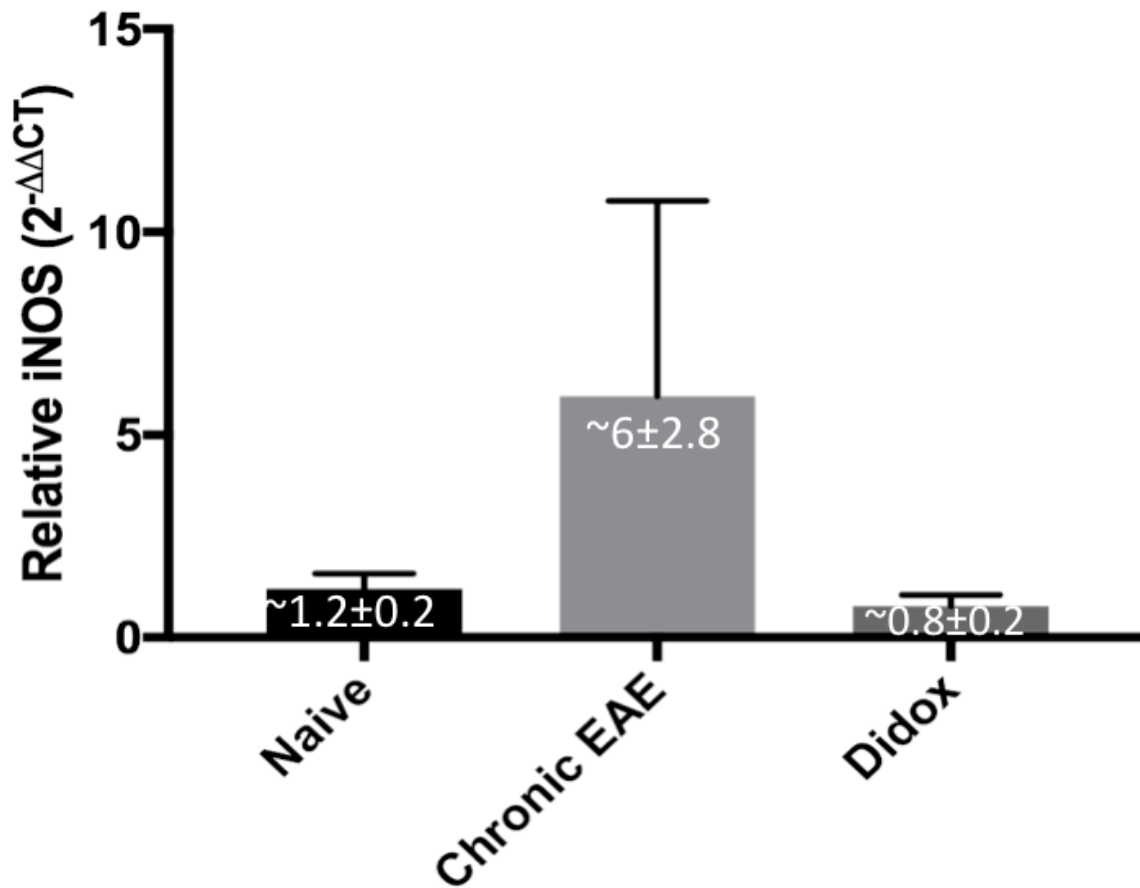


Figure 9. iNOS mRNA Levels are Elevated in the Cortex of Chronic EAE Mice. Average cortical mRNA levels of iNOS rise in Chronic EAE mice relative to Naïve mice (compare Chronic EAE at 6 ± 2.8 vs. Naïve at 1.2 ± 0.2) and decrease following treatment with Didox (Didox expression is 0.8 ± 0.2). No statistical difference between treatment groups was detected (one-way ANOVA, $n = 3$ at each time point).

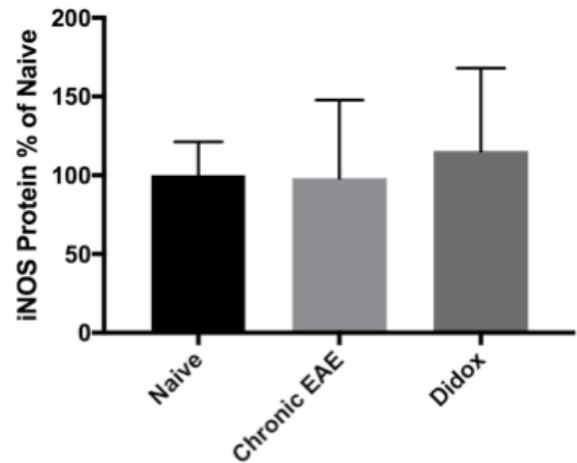
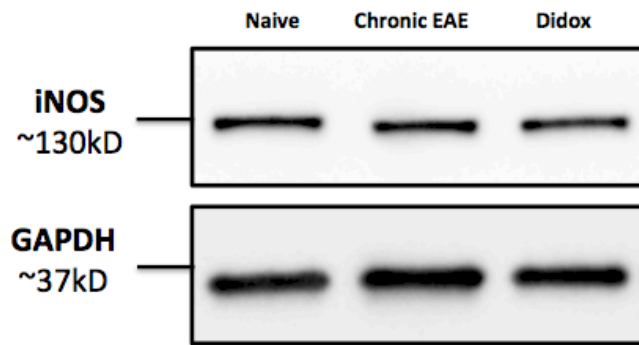


Figure 10. iNOS protein levels are not changed in Chronic EAE mice. Western blot analysis and densitometry of iNOS immunoreactive bands in cortical lysates revealed no significant change in protein levels of iNOS (one-way ANOVA, n=3 at each time point).

β IV spectrin protein levels are not altered in EAE

Although vital for the initial setup of the AIS, Ankyrin-G is a relatively fast-changing portion of the initial segment with a half life of ~ 7 days in vitro (Hedstrom et al., 2008). β IV spectrin has an in vitro half life of ~ 2 weeks and is regarded as essential for both the function and long term stability of the initial segment (Hedstrom et al., 2008; Komada and Soriano, 2002; Yang et al., 2007). In order to further characterize the Chronic EAE model we also performed western blots analysis for β IV spectrin. Decreasing β IV spectrin protein levels in western blots concurrent with loss of Ankyrin-G observed in immunocytochemistry would indicate the loss of two key initial segment proteins and lend support to the idea of AIS breakdown in Chronic EAE.

As previously reported, two bands were observed for β IV spectrin corresponding to the two alternatively spliced variants present at the initial segment (Berghs et al., 2000; Lacas-Gervais et al., 2004; Yang et al., 2007). β IV spectrin $\Sigma 1$, is the essential spectrin for AIS stability, was observed by western blot analysis and identified at ~ 250 kD, while β IV spectrin $\Sigma 6$ was observed at ~ 150 kD (Lacas-Gervais et al., 2004; Yang et al., 2007). Densitometry was performed and compared to GAPDH loading controls. Levels of β IV spectrin were not found to be significantly different in any of the experimental groups (Figure 11).

In addition to showing a reduction of full length β IV spectrin in a stroke model, Schafer et al. (2009) reported the presence of a β IV spectrin breakdown product at ~ 45 kD. The presence of this breakdown product would support AIS disruption. Therefore, we determined to use the presence or absence of this breakdown product to further assess β IV spectrin integrity. As shown in Figure 11, no difference in the intensity of β IV spectrin⁺ bands at the appropriate size was observed.

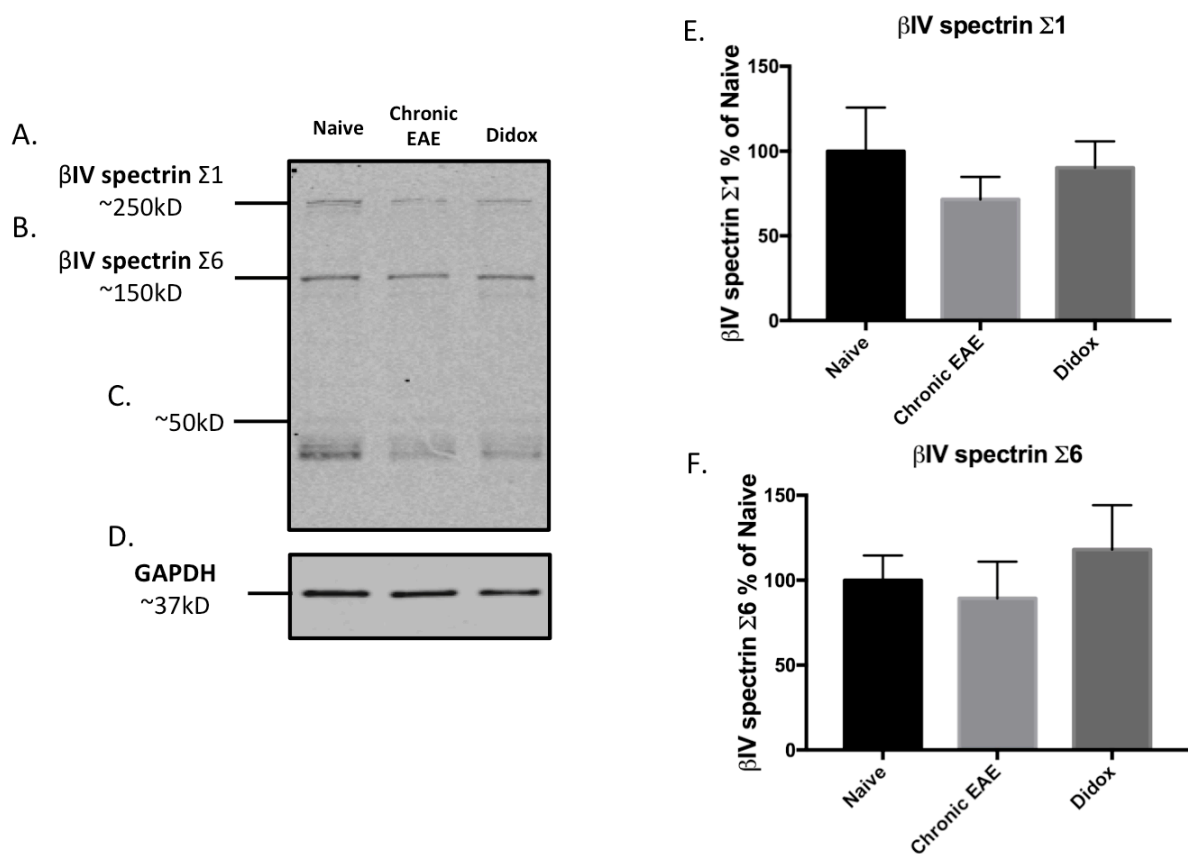


Figure 11. β IV spectrin protein levels are not changed in Chronic EAE mice. Western Blot Analysis and densitometry of β IV spectrin immunoreactive bands from cortical lysates revealed no significant change in protein levels of either of the alternatively spliced variants present at the initial segment (A,B,E,F). In addition, no difference in the intensity of visible bands was detected among any of the treatment groups at ~45kD (C). All protein levels are relative to the GAPDH loading control (D) (one-way ANOVA, $n=3$ at each time point).

Chapter 4: LPS Induced Inflammation Results

LPS-mediated inflammation induces AIS shortening and loss which recovers at a chronic time point

Our studies attempt to determine whether the effects of inflammation on AIS integrity are reversible. In order to determine the effects of inflammation on the AIS, we also employed the well-characterized model of inflammation called LPS-mediated inflammation. Unlike EAE, LPS-mediated inflammation follows a predictable physiological progression with limited variability among animals. Previous studies from our laboratory using the LPS-induced inflammation model have established that a single peripheral injection of LPS induces a significant rise in CNS inflammatory markers within 6 hours, and results in a significant decrease in AIS number by 24 hours post-injection (Benusa and Dupree, unpublished observations). This loss in AIS number persists through 1-week post LPS injection, and is accompanied by persistent cortical inflammation. Qualitative analysis of immunolabeling for CD4+ T-cells in the cortex indicates that there is not widespread T-cell infiltration in LPS-mediated inflammation (Benusa and Dupree, unpublished observations).

Animals were treated with the anti-inflammatory Didox beginning 1-week post LPS injection and AIS stability was analyzed 1 week later (2 weeks post-LPS injection). AIS quantitation, based on the automated counting method (see Chapter 6), revealed a significant reduction of initial segments in 1 Week LPS mice ($34.7 \pm 5.1\%$ average loss) compared to Controls. Surprisingly, AIS numbers were significantly increased back to control levels in 2 Weeks LPS mice ($12.9 \pm 2.7\%$ loss) independent of anti-inflammatory Didox treatment (Figure

12, A-C, E). No significant change in the number of initial segments was detected with Didox treatment when compared to saline controls ($8.1 \pm 2.7\%$ loss) (Figure 12, A,D,E). However, AIS length analysis revealed a significant decrease at both the 1 Week LPS and 2 Week LPS time points (compare an average Control length of $16.8 \pm 0.4 \mu\text{m}$ to $15.3 \pm 0.1 \mu\text{m}$ for 1 Week LPS animals and $15.6 \pm 0.2 \mu\text{m}$ for 2 Week LPS animals) (Figure 12, F). Didox treated animals displayed an average AIS length of $16.2 \pm 0.1 \mu\text{m}$, which is not significantly different from the average control length of $16.8 \pm 0.4 \mu\text{m}$. One-way ANOVA did not reveal a significant difference between Didox AIS length and 2 Week LPS length.

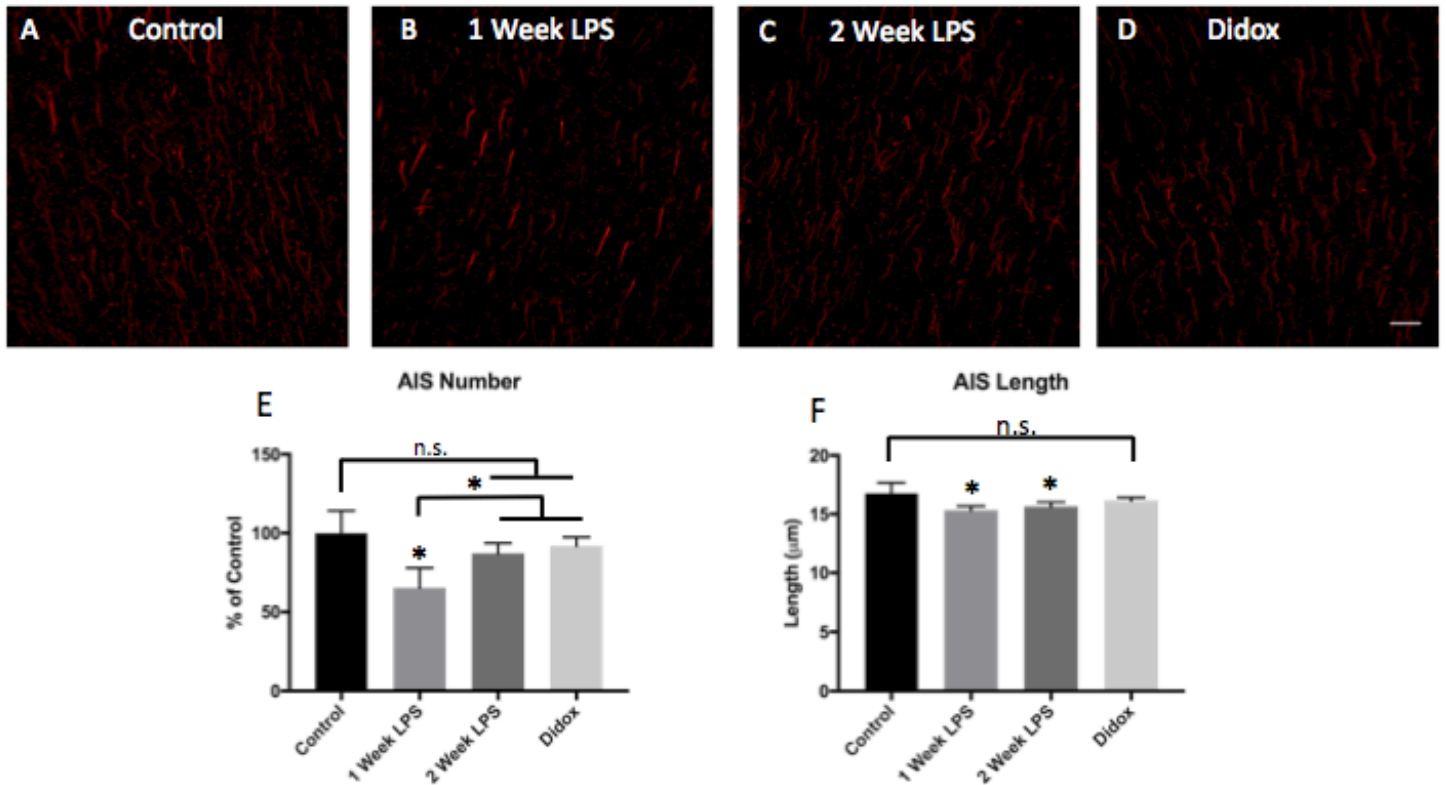


Figure 12. LPS-mediated inflammation induces significant loss of AIS number and length. AIS numbers are significantly reduced 1-week post LPS injection and recover independently of Didox treatment 2-weeks post injection (A-D, E). AIS length is significantly reduced 1-week post-LPS injection and remains shortened at the 2-week time point. Average AIS length and number for Didox treated animals are not significantly different from Control (n=4-6 per treatment group, one-way ANOVA, $p < 0.05$, scale bar=20µm).

Microglia display a less reactive morphology in 2 Week LPS animals.

Since our hypothesis implicates reactive microglia as the driving force for AIS pathology following inflammation, we qualitatively assessed microglia reactivity based on morphology. Qualitative analysis of microglia morphology revealed that compared to Control animals, microglia are reactive in 1 Week LPS animals, but show decreased reactivity in both 2 Week LPS and Didox animals (Figure 13). This mirrors the EAE studies and is consistent with the possibility that microglia mediated inflammation may drive the observed changes in the initial segments.

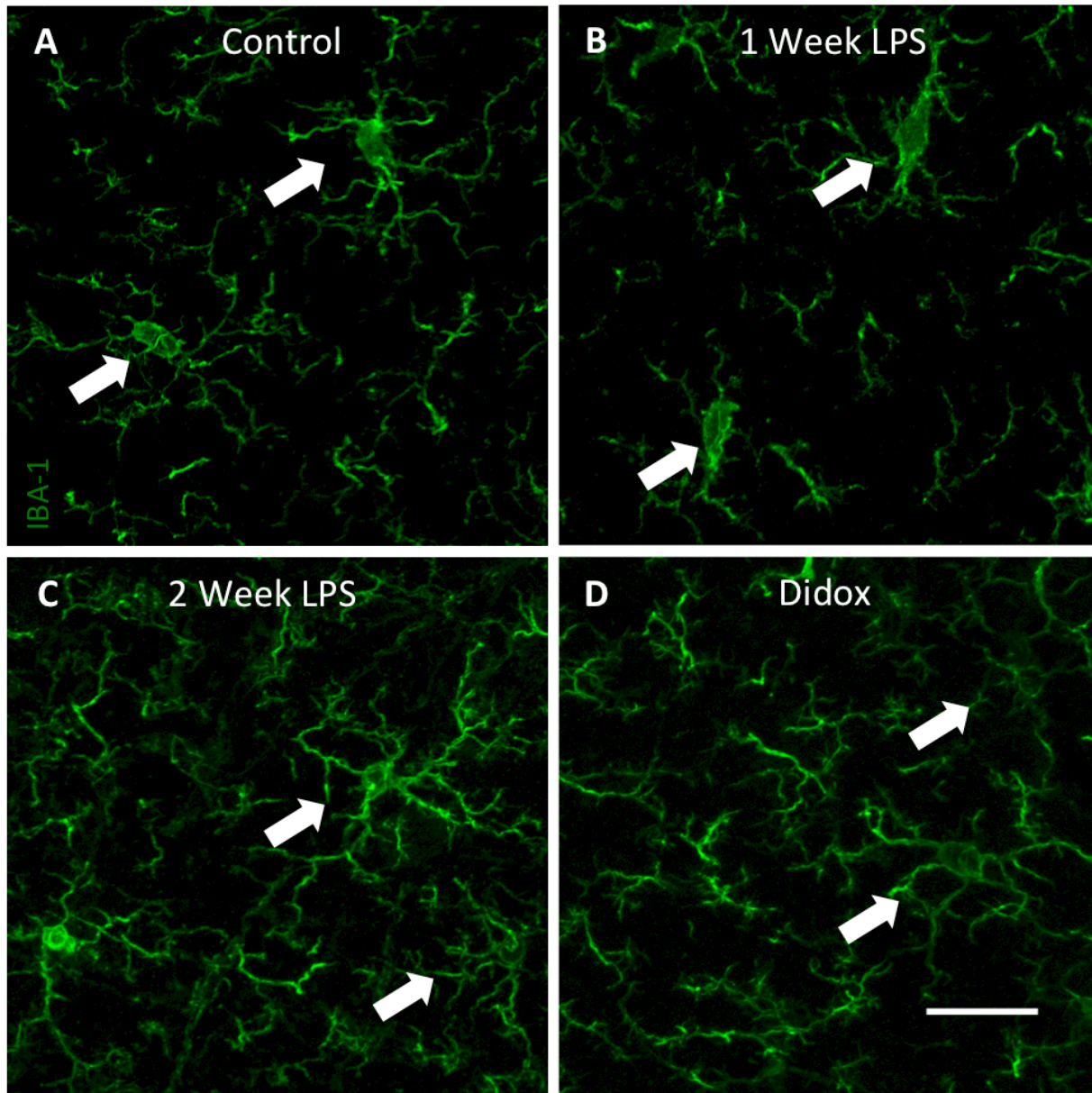


Figure 13. Microglia reactivity in LPS-mediated inflammation. Microglia display a ramified, surveying phenotype in Control mice (A). Microglia adopt a reactive morphology in 1-Week LPS mice, displaying larger cell bodies and shorter, thicker, branches (B). Microglia reactivity decreases in 2-Week LPS and in Didox mice (C,D)(scale bar=20 μ m).

Neuron cell count is not changed in LPS-mediated inflammation.

To determine if the reduction in AIS number was a consequence of neuron cell loss, brain sections were stained with NeuN. There was an average NeuN+ cell count of 242.3 ± 27.6 NeuN+/FOV for Control mice, 228.3 ± 18 NeuN+/FOV for 1 Week LPS animals, 244.5 ± 26.2 NeuN+/FOV for 2 Week LPS animals, and 232 ± 20.8 NeuN+/FOV for Didox treated animals. There was no significant difference in NeuN+ cells among any of the treatment groups (Figure 14).

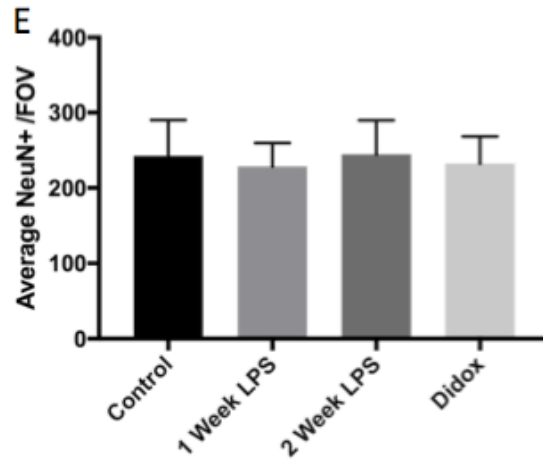
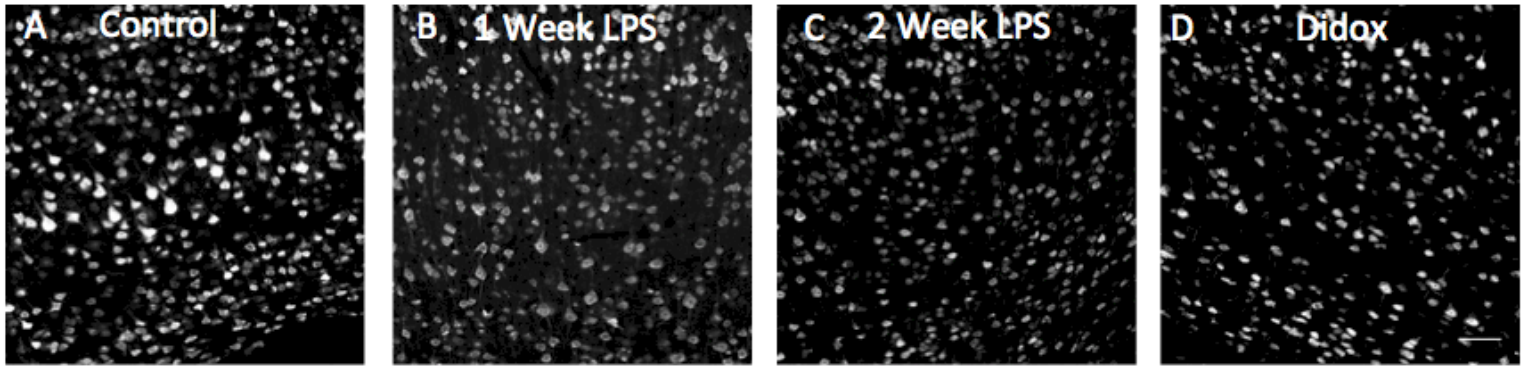


Figure 14. NeuN+ nuclei loss is not detected in LPS-mediated inflammation. NeuN was used to label neuronal nuclei in Control (A), 1 Week LPS (B), 2 Week LPS (C), and Didox (D) animals. Group means were compared using one-way ANOVA and no significant changes were detected (E) (n=3 at each time point, scale bar= 50 μ m).

Chapter 5: Discussion

Changes in AIS number are observed in Chronic EAE, but these changes are not significant.

We have previously reported that initial segment length is significantly reduced in Early EAE, and this decrease in length is followed by a significant loss in the number of initial segments at the Late EAE time point. Treatment with the anti-inflammatory Didox led to a significant recovery in the number of initial segments present in Late EAE animals (Clark et al., 2016). These results indicated an ability to ameliorate initial segment disruption. In the current study, we sought to test the ability of Didox to reverse the loss of initial segments at a time point when there had previously been a significant loss. Here, we report an average initial segment loss of $37 \pm 10.4\%$ at a Late EAE time point compared to naive controls, and mice at the Chronic EAE time point displayed an average loss of $43.5 \pm 11.6\%$. Mice treated with anti-inflammatory Didox displayed a loss of $21.9 \pm 8.9\%$ when compared to Naive controls, or $\sim 20\%$ more initial segments than untreated animals. Although a trend to recover was noted in the Didox treated animals, the results for all groups were not significantly different from Naïve animals. The variability of the EAE model is highlighted by these results. The final analysis of initial segment number and length was composed of 8 Chronic EAE mice, 7 Didox mice, 4 Late EAE mice, and 4 Naïve mice. Based on a power analysis to detect significance at a level of 0.95 and a power of 0.80, a group size of 5 is required for all EAE time points.

Initial segments spontaneously recover in LPS-mediated inflammation

LPS-mediated inflammation was used to investigate the effects of prolonged inflammation on the AIS independently of blood brain barrier breakdown and T-cell infiltration. Although the blood brain barrier is preserved following LPS injection, peripherally generated

inflammatory cytokines enter the CNS and facilitate an inflammatory response. Using this model, we observed a significant decrease of $34.7 \pm 5.1\%$ in the number of initial segments 1 week following LPS injection compared to Controls. Analysis at the 2 weeks post LPS time point revealed a significant restoration of AISs, with animals displaying a $12.9 \pm 2.7\%$ loss compared to Control. The extent of recovery in Didox treated mice was not significantly different from the non-treated mice (8.1 ± 2.7 loss compared to Control). These results indicate that there is spontaneous recovery of the initial segment 2 weeks post-LPS injection. These findings are highly significant in regard to the potential for AIS recovery. This study is the first to show that the loss of cortical initial segments can be reversed, with the literature stating that the loss of initial segments is irreversible (Schafer et al., 2009). These findings are potentially highly impactful for patients suffering from inflammatory diseases such as MS, as preliminary data indicates that cortical AISs are lost in this devastating disease (Figure 2). Interestingly, the anti-inflammatory drug Didox did not provide a further significant recovery (improved restoration of only $\sim 4\%$). However, it is interesting to note that the length of initial segments are significantly shorter both 1-week after LPS treatment and 2-weeks after LPS treatment when compared to Control. The length of initial segments in Didox treated animals is not significantly different from the length of Control animals. Recovery may be spontaneous, but the anti-inflammatory effects of Didox may serve to accelerate the recovery. Future experiments will determine whether Didox treatment can reverse the loss of initial segments noted at earlier time points. If Didox does lead to recovery at earlier time points, this would indicate that resolution of inflammation can decrease the normal time course for recovery in LPS-induced inflammation.

Microglia become less reactive in Prolonged Inflammation.

Microglia are the resident immune cells of the CNS and are known to respond to inflammation in EAE and MS by adopting a reactive, or M1 polarized morphology (Gold et al., 2006; Heppner et al., 2005; Kipp et al., 2012; Rawji and Yong, 2013; Taetzsch et al., 2015). We have previously reported that microglia reactivity closely correlates to EAE progression and is resolved following Didox treatment (Clark et al., 2016). A similar tendency is noted in early LPS studies. Surprisingly, assessment of microglia morphology indicates that microglia resolve at the Chronic EAE time point and 2 week post LPS injection time point in both Didox treated and untreated animals. This indicates a resolving inflammatory environment at the end of the EAE and LPS-inflammation studies.

Interestingly, whole cortex lysates reveal increased levels of TNF α at the Chronic EAE time point, and these levels were decreased following treatment with Didox. iNOS levels were also elevated in Chronic EAE animals and decreased following Didox treatment, but these changes were not significant. These results indicate an increased inflammatory environment in Chronic EAE, which resolves following treatment with Didox. These findings seem contrary to the qualitative assessment of microglia morphology, which indicates a resolved inflammatory environment in Didox treated and untreated animals. Our findings support the idea that morphological changes alone do not necessarily portray functional aspects of microglia. Microglia are versatile cells that exist on a spectrum of activity states rather than a binary (inflammatory or surveying) state (Hanisch and Kettenmann, 2007; Taetzsch et al., 2015). Further studies will aim to isolate microglia and analyze mRNA expression profiles to determine if there are differences between microglia at these time points that is not reflected by morphology. The expression of microglia in LPS-induced inflammation will also be assessed to

determine whether they are similar to those seen in Chronic EAE studies, and to further elucidate a mechanism for the loss and recovery of initial segments.

Didox is a broadly acting anti-inflammatory that inhibits cell division through actions as a ribonucleotide reductase inhibitor and it also inhibits the inflammation-associated transcription factor NF κ B (Inayat et al., 2002; Inayat et al., 2010; Matsebatlela et al., 2015; Shah et al., 2015). The effects of Didox are broad, and the precise mechanism for reducing prolonged inflammation in these studies is not clear. Although microglia are suspected to mediate the loss of initial segments, they could also be involved in the recovery seen in LPS-induced inflammation. Didox could also be acting peripherally, on cells that infiltrate the CNS during EAE, or on other cells of the CNS known to produce inflammatory cytokines. Further experiments are required to determine whether Didox acts on microglia to reduce the inflammatory environment in EAE, and whether the same mechanism is responsible for LPS-mediated inflammation model.

Loss of The Axon Initial Segment in Prolonged Inflammation is Reversible.

The studies presented here provide the first evidence that the loss of initial segments in prolonged inflammation is reversible. The AIS is known to be a highly plastic structure, with altered structure reported in response to electrical activity (Evans et al.; Grubb and Burrone, 2010; Kuba et al., 2010) as well as in models of traumatic brain injury (Baalman et al., 2015), stroke (Hinman et al., 2013; Schafer et al., 2009), and EAE (Clark et al., 2016). Although some axonal sprouting was reported in a study of the AIS in white matter stroke (Hinman et al., 2013), recovery of the AIS in the weeks following injury has not been reported (Schafer et al., 2009). Though results from the Chronic EAE study were underpowered, the loss of initial segments observed in LPS-mediated inflammation is reversed in both 2 Week LPS and Didox treated animals. These results indicate that loss of the initial segments in prolonged inflammation is

reversible. What accounts for the recovery of initial segments in these studies? One possibility is that the loss of initial segments is a plastic adaptation in response to inflammation, and the underlying AIS cytoskeleton is not lost at the time points investigated. Western blots indicate that both major isoforms of β IV spectrin are not decreased in Chronic EAE. The irreversible loss of initial segments reported in Schafer et al. (2009) was characterized by the presence of a β IV spectrin breakdown product at \sim 45kD. Differences in β IV spectrin⁺ bands at \sim 45kD were not observed in the current study, indicating preservation of the cytoskeleton in Chronic EAE. It is possible that the presence of the β IV spectrin cytoskeleton is necessary for the recovery noted in our study, and loss of the β IV spectrin cytoskeleton observed in Schafer et al. (2009) is an indicator of permanent loss of the initial segment. Further experiments will use immunocytochemistry and western blotting to determine whether the cytoskeleton is also preserved in LPS-mediated inflammation and whether preservation of the AIS cytoskeleton is required for recovery of the initial segment after prolonged inflammation.

Chapter 6: Automated Quantitation of Initial Segments and NeuN+ Cells

Automating Image Processing and Quantitation

An established manual counting method, discussed previously, was used for EAE initial segment quantitation (Clark et al., 2016) For the LPS study, I developed a semi-automated method for pre-processing images and counting initial segments and nuclei using custom macros and Plugins included in the FIJI (FIJI is just ImageJ) distribution of the NIH's ImageJ software (Schneider et al., 2012). A macro is a simple program that runs a series of steps automatically (ImageJ). Though simple, macros can be a powerful tool for quickly and accurately analyzing large collections of data. Steps of the semi- automated analysis are as follows: Preprocessing, quantification, raw data filtering and traditional statistical analysis.

Preprocessing

Raw images are processed into a format easily manipulated in bulk using ImageJ. It is important that the original images from the microscope are preserved in the proprietary format in order to preserve the metadata for publication and more detailed analysis.

1. Save the images in the proprietary image format of the microscope (i.e. “.czi” or “.lsm” for Zeiss® software) to preserve the metadata and the complete image data. Then, create a maximum intensity projection saved as a tiff file with identifying information including (as applicable): Animal ID, treatment, cohort, slice, and image number.
2. Move all maximum projections to a folder for batch processing. To split large batches of channels, an ImageJ macro called *SplitChannelMacro* was developed.

3. The *SplitChannelMacro* works by automating the following steps normally taken when splitting channels of a multi-channel microscope image. *SplitChannelMacro*:
- a. Creates new folders for split images called “RedChannel” and “GreenChannel”.
 - b. Selects an image, runs the ImageJ *Split Channel* command.
 - c. Saves only the relevant channel with a new identifier (“red_” or “green_” for our purposes) to the appropriate “RedChannel” or “GreenChannel” folder while discarding other channels (the macro can be modified to save any or all channels).
 - d. Progress can be monitored in the ImageJ log screen and “One Channel Conversion is Complete” is printed on the screen upon once a loop is completed.

A version of the *SplitChannelMacro* used in the analysis of the LPS data is shown in Figure 15.

```

//SplitChannelMacro
    inputFolder= getDirectory("Choose a Directory");
    print(inputFolder);
    outputRed= inputFolder + "/RedChannel/";
    outputGreen= inputFolder + "/GreenChannel/";
    images= getFileList(inputFolder);
    File.makeDirectory(outputRed);
    File.makeDirectory(outputGreen);

    for (i=0; i<images.length; i++) {
        inputPath= inputFolder + images[i];
        open (inputPath);
        imageName=getTitle();
        print("Splitting Image: " + imageName);
        run("Split Channels");
        selectWindow(imageName + " (blue)");
        close();
        selectWindow(imageName + " (green)");
        saveAs("Tiff", outputGreen + "green_" +imageName);
        close();
        selectWindow(imageName + " (red)");
        saveAs("Tiff", outputRed + "red_" +imageName);
        close();
        write("Conversion Complete");
    }

```

} A
} B
} C

Figure 15. SplitChannelMacro explained. This simple macro automates channel splitting of maximum intensity projection “.tiff” files. First, the macro prompts the user to choose a directory containing the images and creates new folders for the processed images (A). Then, a loop is initiated to process all images in the directory (B). The FIJI split channel command is then executed and the relevant images are saved (C). This version saves the “green” and “red” channel into the appropriate folders. It can easily be modified to save any or all channels. This macro is written for use in ImageJ/FIJI.

Quantitation

Quantitation of initial segments requires a consistent threshold method for images and the *Analyze Particles* Plugin distributed with FIJI. A threshold is applied to images, *Analyze Particles* is run, and the output data is filtered and all particles less than 10 μ m are excluded before the final analysis. This length exclusion was set for this study and can be modified to be more inclusive. Length is determined using the “Feret’s diameter” option. Feret’s diameter is the caliper diameter of the object selected by *Analyze Particles*. In FIJI, Feret’s diameter refers to the maximum caliper diameter of the object (<https://imagej.nih.gov/ij/docs/guide/146-30.html>) (Schneider et al., 2012). Since initial segments are typically linear objects, Feret’s diameter was tested and considered an appropriate estimate of length (not shown). Because later data processing steps require filtering by length, it is important to set a global scale for the images before processing. This can be found under *Analyze> Set Scale*. The scale is listed in the meta-data of the original microscope image. Several Plugins are available to threshold images in ImageJ (Otsu, Maximum Entropy, Triangle, etc.) (“A Threshold Selection Method” 1979, Landini). After comparing several methods for accuracy based on manual counts, we decided to use the Otsu threshold method for the LPS study. Otsu threshold comes as a pre-installed option in FIJI (“A Threshold Selection Method” 1979, Landini). After a threshold is applied to the images, measurements are set in the *Analyze Particles* Plugin, and a macro is made using the *Record* option in FIJI under the Plugins menu. *Plugins>Macro>Record* allows simple ImageJ macros to be created with no coding required. Simply record the steps that you normally take in image processing and save the resulting commands generated in the *Record* window. For the purposes of this study, the *Threshold* and *Analyze Particles* selections were recorded.

Finding proper settings for the *Analyze Particles* Plugin is essential to using this method for automated analysis. Settings depend on average image quality and require some troubleshooting while developing the macro for specific needs. The macro saves overlay for all images so any anomalies or questionable results can be manually inspected. Settings were evaluated for accuracy by comparing to manual counting of the target particle and by visual inspection of output overlay masks. Once the settings are determined for an experiment, they should be used consistently for all images in that study. The settings and macro used for Ankyrin-G quantification are listed in Figure 16, A, while those used for NeuN are listed in Figure 16, B.

A Initial Segment Automated Quantitation Settings and macro.

```
run("Auto Threshold", "method=Otsu
white");
run("Analyze Particles...",
"circularity=0-0.5 show=[Overlay Masks]
display exclude");
close();
```

Size (μm^2)	0-Infinity
Circularity	0-0.5
Show	Overlay Masks
Display Results	YES
Exclude on edges	YES

B Neuron Nuclei Automated Quantitation Settings

```
run("Auto Threshold", "method=Otsu
white");
run("Analyze Particles...", "size=10-150
show=[Overlay Masks] display exclude");
close();
```

Size (μm^2)	10-150
Circularity	0-1
Show	Overlay Masks
Display Results	YES
Exclude on edges	YES

Figure 16. Macro and settings for automated quantitation. Settings were optimized for accuracy for initial segment and neuronal nuclei quantitation. Once established, settings must be kept consistent throughout analysis. Settings and the macro are provided for initial segment quantitation (A), and neuronal nuclei quantitation (B).

Once the macro is created, it can be saved as a text file and installed in FIJI for launch on startup. Macros can also be used from the raw text form to batch file analysis using the *Process>Batch>Macro...* command in FIJI. The latter method was used for this study as the install-ready Plugin is still in development.

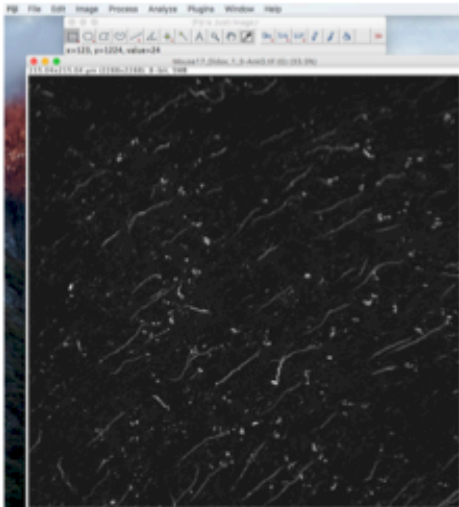
Automated ImageJ steps for quantification:

1. Open an image and set the global scale.
2. Open image for analysis.
3. Apply threshold to images.
4. Run the Plugin *Analyze Particles* (with proper settings).
5. Filter data.
6. Save for future analysis.

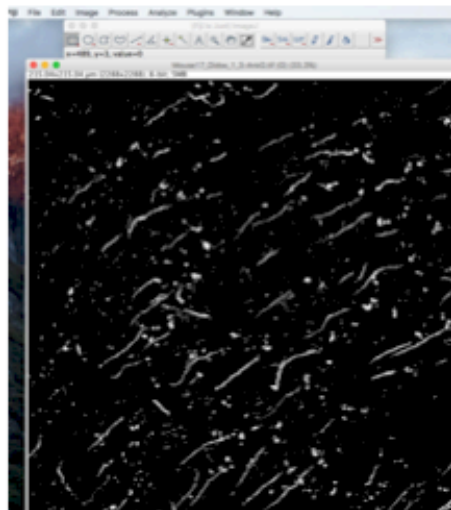
The macro automates steps 2-4. The pre-determined settings for image threshold and *Analyze Particles* are built into the macro, and the global scale only needs to be set once per analysis session. Sample input, threshold, and output images and measures are shown in Figure 17.

Manual counts performed for a sample of three saline animals resulted in an average of 85.6 ± 4.7 AISs/Field of view (FOV). Automated counts for these same animals resulted in 97.7 ± 11.1 AISs/FOV (Figure 18). A t-test comparing the values for each mouse revealed no statistical difference between the two counting methods. This comparison was repeated with 3 other time points and no difference was detected between manual and automated counts (not shown).

A Input Image



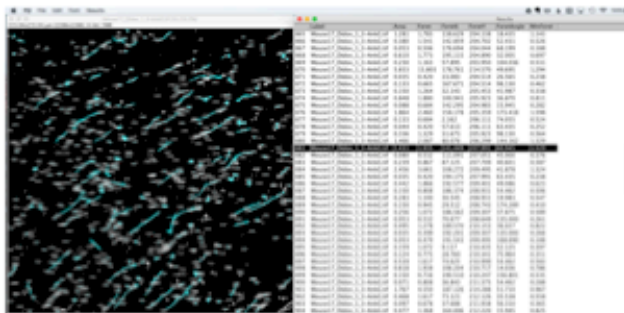
B Post-threshold Image



Otsu
Threshold.



C Output From *Analyze Particles*



D Filter results by size

Pre-filter: 911 AISs

R Code:

```
Library(dplyr)
```

```
Filtered<- Filter(Data, Feret>=10)
```

Post Filter: 38 AIS.



Figure 17. Procedure for automated image quantitation. First, the Otsu threshold is applied to the image (A,B). Then, Analyze Particles is run. Output overlay mask and data are shown (C). Results are then filtered by size using R (D), or Microsoft Excel (not shown).

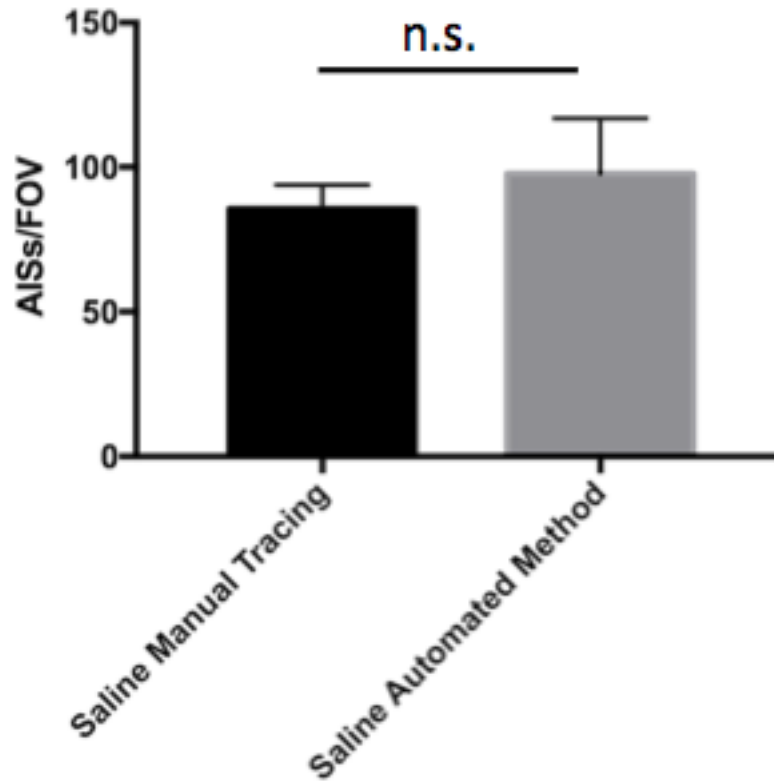


Figure 18. No difference is detected between automated counting method and manual counting. A t-test was performed to compare the amount of initial segments counted manually to the new automated method of counting. No difference was detected between the two methods. This assessment was repeated with three other paired groups and no difference was detected between manual and automated counting in any group (not shown).

Limitations and Conclusions

This semi-automated method greatly speeds up image analysis without sacrificing the accuracy of manual counting. Analysis can now be performed as soon as images are taken. Automation and standard image thresholds also removes user bias, and improves consistency by removing inter-user discrepancies-- anyone running the program will get the same results. As with any automated process, there are limitations. This process in particular requires images with high signal to noise ratios-- antigen retrieval techniques and linear unmixing are recommended. There are also inherent limitations when using maximum intensity projections to analyze 3-dimensional images. Initial segments overlapping in the z-plane may be counted together, artificially lowering the true number of initial segments. This is a limitation for both manual and automated counting methods, though a qualitative assessment revealed that the degree of overlap was minimal in layer V of the cortex. Also, while initial segments touching the four lateral edges of the image are excluded by the *Analyze Particles* Plugin, there is currently not a way to exclude initial segments that may pass in or out of the top or bottom edges of the image. This problem was noted in Hinman et al. (2013) when the *NeuronJ* Plugin for FIJI was used to measure initial segments. Although this is a concern, the lack of a significant difference between manual counting methods which exclude initial segments touching the top or bottom of the stack and this automated method leads us to believe that the proportion of AISs passing through the top or bottom of the z-plane is similar between groups or negligible (Figure 18).

The program also picks up a very large number of short particles that are clearly not initial segments when manually inspected. This is addressed using the data processing step in which the initial segments are filtered by size and anything that is less than 10 μm in length is

excluded. After filtering and a comparison to manually processed images, the number of initial segments counted with the automated method is not statistically different from the amount counted manually (Figure 18). Although we have not yet found a method to completely exclude initial segments that pass the filtering step but still pass out of the z-plane, the precision of automated counts when compared to the established manual method, and the advantages in speed and consistency led us to adopt the method for LPS studies. Future versions of this method will attempt to address the limitations. Macros, methods, updates, and future Plugin development will be stored and maintained in a Github repository (<https://github.com/nkicg6>) for download.

List of References

1. (1979). A Threshold Selection Method from Gray-Level Histograms. *IEEE Transactions on Systems, Man, and Cybernetics* 9, 62-66.
2. National MS Society. Multiple Sclerosis.2016, <http://www.nationalmssociety.org/Symptoms-Diagnosis>
3. Amor, V., Feinberg, K., Eshed-Eisenbach, Y., Vainshtein, A., Frechter, S., Grumet, M., Rosenbluth, J., and Peles, E. (2014). Long-term maintenance of Na⁺ channels at nodes of Ranvier depends on glial contact mediated by gliomedin and NrCAM. *J. Neurosci.* 34, 5089-5098.
4. Azevedo, F.A., Carvalho, L.R., Grinberg, L.T., Farfel, J.M., Ferretti, R.E., Leite, R.E., Jacob Filho, W., Lent, R., and Herculano-Houzel, S. (2009). Equal numbers of neuronal and nonneuronal cells make the human brain an isometrically scaled-up primate brain. *J. Comp. Neurol.* 513, 532-541.
5. Baalman, K., Marin, M.A., Ho, T.S., Godoy, M., Cherian, L., Robertson, C., and Rasband, M.N. (2015). Axon initial segment-associated microglia. *J. Neurosci.* 35, 2283-2292.
6. Bennett, V., and Baines, A.J. (2001). Spectrin and ankyrin-based pathways: metazoan inventions for integrating cells into tissues. *Physiol. Rev.* 81, 1353-1392.
7. Berghs, S., Aggujaro, D., Dirx, R., Jr, Maksimova, E., Stabach, P., Hermel, J.M., Zhang, J.P., Philbrick, W., Slepnev, V., Ort, T., and Solimena, M. (2000). betaIV spectrin, a new spectrin localized at axon initial segments and nodes of ranvier in the central and peripheral nervous system. *J. Cell Biol.* 151, 985-1002.
8. Bjartmar, C., Kinkel, R.P., Kidd, G., Rudick, R.A., and Trapp, B.D. (2001). Axonal loss in normal-appearing white matter in a patient with acute MS. *Neurology* 57, 1248-1252.
9. Blaylock, R.L. (2013). Immunology primer for neurosurgeons and neurologists part 2: Innate brain immunity. *Surg. Neurol. Int.* 4, 118-7806.118349.
10. Boche, D., Perry, V.H., and Nicoll, J.A. (2013). Review: activation patterns of microglia and their identification in the human brain. *Neuropathol. Appl. Neurobiol.* 39, 3-18.
11. Britt, D.J., Farias, G.G., Guardia, C.M., and Bonifacino, J.S. (2016). Mechanisms of Polarized Organelle Distribution in Neurons. *Front. Cell. Neurosci.* 10, 88.

12. Castelfranco, A.M., and Hartline, D.K. (2016). Evolution of rapid nerve conduction. *Brain Res.*
13. Christmas, P. (2010). Toll-Like Receptors: Sensors that Detect Infection. *2016*,
<http://www.nature.com/scitable/topicpage/toll-like-receptors-sensors-that-detect-infection-14396559>
14. Clark, K.C., Josephson, A., Benusa, S.D., Hartley, R.K., Baer, M., Thummala, S., Joslyn, M., Sword, B.A., Elford, H., Oh, U., *et al.* (2016). Compromised axon initial segment integrity in EAE is preceded by microglial reactivity and contact. *Glia* (Epub ahead of print).
15. Constantinescu, C.S., Farooqi, N., O'Brien, K., and Gran, B. (2011). Experimental autoimmune encephalomyelitis (EAE) as a model for multiple sclerosis (MS). *Br. J. Pharmacol.* *164*, 1079-1106.
16. Davis, J.Q., McLaughlin, T., and Bennett, V. (1993). Ankyrin-binding proteins related to nervous system cell adhesion molecules: candidates to provide transmembrane and intercellular connections in adult brain. *J. Cell Biol.* *121*, 121-133.
17. Deerinck, T.J., Levinson, S.R., Bennett, G.V., and Ellisman, M.H. (1997). Clustering of voltage-sensitive sodium channels on axons is independent of direct Schwann cell contact in the dystrophic mouse. *J. Neurosci.* *17*, 5080-5088.
18. Dupree, J.L., Mason, J.L., Marcus, J.R., Stull, M., Levinson, R., Matsushima, G.K., and Popko, B. (2004). Oligodendrocytes assist in the maintenance of sodium channel clusters independent of the myelin sheath. *Neuron. Glia Biol.* *1*, 179-192.
19. Dupree, J.L., Polak, P.E., Hensley, K., Pelligrino, D., and Feinstein, D.L. (2015). Lanthionine ketimine ester provides benefit in a mouse model of multiple sclerosis. *J. Neurochem.* *134*, 302-314.
20. Evans, M., Dumitrescu, A., Kruijssen, D.H., Taylor, S., and Grubb, M. Rapid Modulation of Axon Initial Segment Length Influences Repetitive Spike Firing. *Cell Reports*, *13*(6), pp.1233-1245.
21. Fache, M.P., Moussif, A., Fernandes, F., Giraud, P., Garrido, J.J., and Dargent, B. (2004). Endocytotic elimination and domain-selective tethering constitute a potential mechanism of protein segregation at the axonal initial segment. *J. Cell Biol.* *166*, 571-578.

22. FarÅas, G.G., Cuitino, L., Guo, X., Ren, X., Jarnik, M., Mattera, R., and Bonifacino, J.S. (2012). Signal-mediated, AP-1/Clathrin-dependent Sorting of Transmembrane Receptors to the Somatodendritic Domain of Hippocampal Neurons. *Neuron* 75, 810-823.
23. Fukushima, S., Furube, E., Itoh, M., Nakashima, T., and Miyata, S. (2015). Robust increase of microglia proliferation in the fornix of hippocampal axonal pathway after a single LPS stimulation. *J. Neuroimmunol.* 285, 31-40.
24. Galiano, M.R., Jha, S., Ho, T.S., Zhang, C., Ogawa, Y., Chang, K.J., Stankewich, M.C., Mohler, P.J., and Rasband, M.N. (2012). A distal axonal cytoskeleton forms an intra-axonal boundary that controls axon initial segment assembly. *Cell* 149, 1125-1139.
25. Ghasemi, M., and Fatemi, A. (2014). Pathologic role of glial nitric oxide in adult and pediatric neuroinflammatory diseases. *Neurosci. Biobehav. Rev.* 45, 168-182.
26. Gold, R., Linington, C., and Lassmann, H. (2006). Understanding pathogenesis and therapy of multiple sclerosis via animal models: 70 years of merits and culprits in experimental autoimmune encephalomyelitis research. *Brain* 129, 1953-1971.
27. Grubb, M.S., and Burrone, J. (2010). Activity-dependent relocation of the axon initial segment fine-tunes neuronal excitability. *Nature* 465, 1070-1074.
28. Hamada, M.S., and Kole, M.H. (2015). Myelin loss and axonal ion channel adaptations associated with gray matter neuronal hyperexcitability. *J. Neurosci.* 35, 7272-7286.
29. Hanisch, U.K., and Kettenmann, H. (2007). Microglia: active sensor and versatile effector cells in the normal and pathologic brain. *Nat. Neurosci.* 10, 1387-1394.
30. Hassel, B., Rathjen, F.G., and Volkmer, H. (1997). Organization of the neurofascin gene and analysis of developmentally regulated alternative splicing. *J. Biol. Chem.* 272, 28742-28749.
31. Hedstrom, K.L., Ogawa, Y., and Rasband, M.N. (2008). AnkyrinG is required for maintenance of the axon initial segment and neuronal polarity. *J. Cell Biol.* 183, 635-640.

32. Heneka, M.T., Klockgether, T., and Feinstein, D.L. (2000). Peroxisome proliferator-activated receptor-gamma ligands reduce neuronal inducible nitric oxide synthase expression and cell death in vivo. *J. Neurosci.* *20*, 6862-6867.
33. Heppner, F.L., Greter, M., Marino, D., Falsig, J., Raivich, G., Hovelmeyer, N., Waisman, A., Rulicke, T., Prinz, M., Priller, J., Becher, B., and Aguzzi, A. (2005). Experimental autoimmune encephalomyelitis repressed by microglial paralysis. *Nat. Med.* *11*, 146-152.
34. Hinman, J.D., Rasband, M.N., and Carmichael, S.T. (2013). Remodeling of the axon initial segment after focal cortical and white matter stroke. *Stroke* *44*, 182-189.
35. Horton, A.C., and Ehlers, M.D. (2004). Secretory trafficking in neuronal dendrites. *Nat. Cell Biol.* *6*, 585-591.
36. Hoshino, K., Takeuchi, O., Kawai, T., Sanjo, H., Ogawa, T., Takeda, Y., Takeda, K., and Akira, S. (1999). Cutting edge: Toll-like receptor 4 (TLR4)-deficient mice are hyporesponsive to lipopolysaccharide: evidence for TLR4 as the Lps gene product. *J. Immunol.* *162*, 3749-3752.
37. Huang, Y.H., Tsai, K., Ma, C., Vallance, B.A., Priatel, J.J., and Tan, R. (2014). SLAM-SAP signaling promotes differentiation of IL-17-producing T cells and progression of experimental autoimmune encephalomyelitis. *J. Immunol.* *193*, 5841-5853.
38. Huber, M., Heink, S., Pagenstecher, A., Reinhard, K., Ritter, J., Visekruna, A., Guralnik, A., Bollig, N., Jeltsch, K., Heinemann, C., *et al.* (2013). IL-17A secretion by CD8+ T cells supports Th17-mediated autoimmune encephalomyelitis. *J. Clin. Invest.* *123*, 247-260.
39. ImageJ, M. ImageJ Macro Language. 2016, <http://rsb.info.nih.gov/ij/developer/macro/macros.html>
40. Inayat, M.S., Chendil, D., Mohiuddin, M., Elford, H.L., Gallicchio, V.S., and Ahmed, M.M. (2002). Didox (a novel ribonucleotide reductase inhibitor) overcomes Bcl-2 mediated radiation resistance in prostate cancer cell line PC-3. *Cancer. Biol. Ther.* *1*, 539-545.
41. Inayat, M.S., El-Amouri, I.S., Bani-Ahmad, M., Elford, H.L., Gallicchio, V.S., and Oakley, O.R. (2010). Inhibition of allogeneic inflammatory responses by the Ribonucleotide Reductase Inhibitors, Didox and Trimidox. *J. Inflamm. (Lond)* *7*, 43-9255-7-43.

42. Jenkins, S.M., and Bennett, V. (2001). Ankyrin-G coordinates assembly of the spectrin-based membrane skeleton, voltage-gated sodium channels, and L1 CAMs at Purkinje neuron initial segments. *J. Cell Biol.* *155*, 739-746.
43. Kettenmann, H., Kirchhoff, F., and Verkhratsky, A. (2013). Microglia: new roles for the synaptic stripper. *Neuron* *77*, 10-18.
44. Kipp, M., Clarner, T., Dang, J., Copray, S., and Beyer, C. (2009). The cuprizone animal model: new insights into an old story. *Acta Neuropathol.* *118*, 723-736.
45. Kipp, M., van der Star, B., Vogel, D.Y., Puentes, F., van der Valk, P., Baker, D., and Amor, S. (2012). Experimental in vivo and in vitro models of multiple sclerosis: EAE and beyond. *Mult Scler. Relat. Disord.* *1*, 15-28.
46. Kizhatil, K., Yoon, W., Mohler, P.J., Davis, L.H., Hoffman, J.A., and Bennett, V. (2007). Ankyrin-G and beta2-spectrin collaborate in biogenesis of lateral membrane of human bronchial epithelial cells. *J. Biol. Chem.* *282*, 2029-2037.
47. Komada, M., and Soriano, P. (2002). BetaIV-spectrin regulates sodium channel clustering through ankyrin-G at axon initial segments and nodes of Ranvier. *J. Cell Biol.* *156*, 337-348.
48. Kordeli, E., Lambert, S., and Bennett, V. (1995). AnkyrinG. A new ankyrin gene with neural-specific isoforms localized at the axonal initial segment and node of Ranvier. *J. Biol. Chem.* *270*, 2352-2359.
49. Kornek, B., Storch, M.K., Weissert, R., Wallstroem, E., Stefferl, A., Olsson, T., Linington, C., Schmidbauer, M., and Lassmann, H. (2000). Multiple sclerosis and chronic autoimmune encephalomyelitis: a comparative quantitative study of axonal injury in active, inactive, and remyelinated lesions. *Am. J. Pathol.* *157*, 267-276.
50. Kuba, H., Oichi, Y., and Ohmori, H. (2010). Presynaptic activity regulates Na(+) channel distribution at the axon initial segment. *Nature* *465*, 1075-1078.
51. Lacas-Gervais, S., Guo, J., Strenzke, N., Scarfone, E., Kolpe, M., Jahkel, M., De Camilli, P., Moser, T., Rasband, M.N., and Solimena, M. (2004). BetaIVSigma1 spectrin stabilizes the nodes of Ranvier and axon initial segments. *J. Cell Biol.* *166*, 983-990.

52. Landini, G. Auto Threshold. http://imagej.net/Auto_Threshold
53. Laroche, C., Uphaus, T., Prat, A., and Zipp, F. (2016). Secondary Progression in Multiple Sclerosis: Neuronal Exhaustion or Distinct Pathology? *Trends Neurosci.* *39*(5), 325-339.
54. Leray, E., Yaouanq, J., Le Page, E., Coustans, M., Laplaud, D., Oger, J., and Edan, G. (2010). Evidence for a two-stage disability progression in multiple sclerosis. *Brain* *133*, 1900-1913.
55. Leterrier, C. (2016). The Axon Initial Segment, 50Years Later: A Nexus for Neuronal Organization and Function. *Curr. Top. Membr.* *77*, 185-233.
56. Li, J., Csakai, A., Jin, J., Zhang, F., and Yin, H. (2016). Therapeutic Developments Targeting Toll-like Receptor-4-Mediated Neuroinflammation. *ChemMedChem* *11*, 154-165.
57. Liu, M., and Bing, G. (2011). Lipopolysaccharide animal models for Parkinson's disease. *Parkinsons Dis.* *2011*, 327089.
58. Matsebatlela, T.M., Anderson, A.L., Gallicchio, V.S., Elford, H., and Rice, C.D. (2015). 3,4-Dihydroxybenzohydroxamic acid (Didox) suppresses pro-inflammatory profiles and oxidative stress in TLR4-activated RAW264.7 murine macrophages. *Chem. Biol. Interact.* *233*, 95-105.
59. Minden, S.L., and Schiffer, R.B. (1990). Affective disorders in multiple sclerosis. Review and recommendations for clinical research. *Arch. Neurol.* *47*, 98-104.
60. Mohler, P.J., Gramolini, A.O., and Bennett, V. (2002). Ankyrins. *J. Cell. Sci.* *115*, 1565-1566.
61. Mullen, R.J., Buck, C.R., and Smith, A.M. (1992). NeuN, a neuronal specific nuclear protein in vertebrates. *Development* *116*, 201-211.
62. Nakada, C., Ritchie, K., Oba, Y., Nakamura, M., Hotta, Y., Iino, R., Kasai, R.S., Yamaguchi, K., Fujiwara, T., and Kusumi, A. (2003). Accumulation of anchored proteins forms membrane diffusion barriers during neuronal polarization. *Nat. Cell Biol.* *5*, 626-632.
63. Nicholson, L.B., Raveney, B.J., and Munder, M. (2009). Monocyte dependent regulation of autoimmune inflammation. *Curr. Mol. Med.* *9*, 23-29.
64. Nimmerjahn, A., Kirchhoff, F., and Helmchen, F. (2005). Resting microglial cells are highly dynamic surveillants of brain parenchyma in vivo. *Science* *308*, 1314-1318.

65. Normand, E.A., and Rasband, M.N. (2015). Subcellular patterning: axonal domains with specialized structure and function. *Dev. Cell.* 32, 459-468.
66. Pan, Z., Kao, T., Horvath, Z., Lemos, J., Sul, J.Y., Cranstoun, S.D., Bennett, V., Scherer, S.S., and Cooper, E.C. (2006). A common ankyrin-G-based mechanism retains KCNQ and NaV channels at electrically active domains of the axon. *J. Neurosci.* 26, 2599-2613.
67. Pomicter, A.D., Shroff, S.M., Fuss, B., Sato-Bigbee, C., Brophy, P.J., Rasband, M.N., Bhat, M.A., and Dupree, J.L. (2010). Novel forms of neurofascin 155 in the central nervous system: alterations in paranodal disruption models and multiple sclerosis. *Brain* 133, 389-405.
68. Qin, L., Wu, X., Block, M.L., Liu, Y., Breese, G.R., Hong, J.S., Knapp, D.J., and Crews, F.T. (2007). Systemic LPS causes chronic neuroinflammation and progressive neurodegeneration. *Glia* 55, 453-462.
69. R Core Team. (2015). R: A Language and Environment for Statistical Computing. R Foundation for Statistical Computing, Vienna, Austria. URL <https://www.R-project.org/>.
70. Ramanathan, S., Dale, R.C., and Brilot, F. (2016). Anti-MOG antibody: The history, clinical phenotype, and pathogenicity of a serum biomarker for demyelination. *Autoimmun. Rev.* 15, 307-324.
71. Rasband, M.N. (2010). The axon initial segment and the maintenance of neuronal polarity. *Nat. Rev. Neurosci.* 11, 552-562.
72. Rasband, M.N., Peles, E., Trimmer, J.S., Levinson, S.R., Lux, S.E., and Shrager, P. (1999). Dependence of nodal sodium channel clustering on paranodal axoglial contact in the developing CNS. *J. Neurosci.* 19, 7516-7528.
73. Rawji, K.S., and Yong, V.W. (2013). The benefits and detriments of macrophages/microglia in models of multiple sclerosis. *Clin. Dev. Immunol.* 2013, 948976.
74. Recks, M.S., Grether, N.B., van der Broeck, F., Ganschler, A., Wagner, N., Henke, E., Ergun, S., Schroeter, M., and Kuerten, S. (2015). Four different synthetic peptides of proteolipid protein induce a distinct antibody response in MP4-induced experimental autoimmune encephalomyelitis. *Clin. Immunol.* 159, 93-106.

75. Richard, J.F., Roy, M., Audoy-Remus, J., Tremblay, P., and Vallieres, L. (2011). Crawling phagocytes recruited in the brain vasculature after pertussis toxin exposure through IL6, ICAM1 and ITGalpham. *Brain Pathol.* *21*, 661-671.
76. Schafer, D.P., Jha, S., Liu, F., Akella, T., McCullough, L.D., and Rasband, M.N. (2009). Disruption of the axon initial segment cytoskeleton is a new mechanism for neuronal injury. *J. Neurosci.* *29*, 13242-13254.
77. Schneider, C.A., Rasband, W.S., and Eliceiri, K.W. (2012). NIH Image to ImageJ: 25 years of image analysis. *Nat. Methods* *9*, 671-675.
78. Shah, K.N., Wilson, E.A., Malla, R., Elford, H.L., and Faridi, J.S. (2015). Targeting ribonucleotide reductase M2 and NF-kappaB activation with Didox to circumvent tamoxifen resistance in breast cancer. *Mol. Cancer. Ther.* *14*(11), 2411-2421.
79. Sherman, D.L., Tait, S., Melrose, S., Johnson, R., Zonta, B., Court, F.A., Macklin, W.B., Meek, S., Smith, A.J., Cottrell, D.F., and Brophy, P.J. (2005). Neurofascins are required to establish axonal domains for saltatory conduction. *Neuron* *48*, 737-742.
80. Sobotzik, J.M., Sie, J.M., Politi, C., Del Turco, D., Bennett, V., Deller, T., and Schultz, C. (2009). AnkyrinG is required to maintain axo-dendritic polarity in vivo. *Proc. Natl. Acad. Sci. U. S. A.* *106*, 17564-17569.
81. Song, A.H., Wang, D., Chen, G., Li, Y., Luo, J., Duan, S., and Poo, M.M. (2009). A selective filter for cytoplasmic transport at the axon initial segment. *Cell* *136*, 1148-1160.
82. Susuki, K., and Rasband, M.N. (2008). Spectrin and ankyrin-based cytoskeletons at polarized domains in myelinated axons. *Exp. Biol. Med. (Maywood)* *233*, 394-400.
83. Szu-Yu Ho, T., and Rasband, M.N. (2011). Maintenance of neuronal polarity. *Dev. Neurobiol.* *71*, 474-482.
84. Taetzsch, T., Levesque, S., McGraw, C., Brookins, S., Luqa, R., Bonini, M.G., Mason, R.P., Oh, U., and Block, M.L. (2015). Redox regulation of NF-kappaB p50 and M1 polarization in microglia. *Glia* *63*, 423-440.
85. Terry, R.L., Ifergan, I., and Miller, S.D. (2016). Experimental Autoimmune Encephalomyelitis in Mice. *Methods Mol. Biol.* *1304*, 145-160.
86. Thummala, S. (2015). Axon Initial Segment Stability in Multiple Sclerosis. *VCU Scholar Compass*

87. Ummenthum, K., Peferoen, L.A., Finardi, A., Baker, D., Pryce, G., Mantovani, A., Bsibsi, M., Bottazzi, B., Peferoen-Baert, R., van der Valk, P., *et al.* (2016). Pentraxin-3 is upregulated in the central nervous system during MS and EAE, but does not modulate experimental neurological disease. *Eur. J. Immunol.* *46*, 701-711.
88. Vabnick, I., Novakovic, S.D., Levinson, S.R., Schachner, M., and Shrager, P. (1996). The clustering of axonal sodium channels during development of the peripheral nervous system. *J. Neurosci.* *16*, 4914-4922.
89. Valentin-Torres, A., Savarin, C., Hinton, D.R., Phares, T.W., Bergmann, C.C., and Stohlman, S.A. (2016). Sustained TNF production by central nervous system infiltrating macrophages promotes progressive autoimmune encephalomyelitis. *J. Neuroinflammation* *13*, 46-016-0513-y.
90. Varatharaj, A., and Galea, I. (2016). The blood-brain barrier in systemic inflammation. *Brain Behav. Immun.*
91. Volk, D.W., and Lewis, D.A. (2005). GABA Targets for the Treatment of Cognitive Dysfunction in Schizophrenia. *Curr. Neuropharmacol.* *3*, 45-62.
92. Wickham, H. (2009). *ggplot2: Elegant Graphics for Data Analysis*. Springer-Verlag New York, 2009.
93. Wickham, H. (2007). Reshaping Data with the reshape Package. *Journal of Statistical Software* *21*, 1-20.
94. Wickham, H., and Francois, R. (2015). *dplyr: A Grammar of Data Manipulation*. R package version 0.4.3. <https://CRAN.R-project.org/package=dplyr>
95. Wu, X.Q., Dai, Y., Yang, Y., Huang, C., Meng, X.M., Wu, B.M., and Li, J. (2016). Emerging role of miRNAs in regulating macrophage activation and polarization in immune response and inflammation. *Immunology*
96. Yang, Y., Lacas-Gervais, S., Morest, D.K., Solimena, M., and Rasband, M.N. (2004). BetaIV spectrins are essential for membrane stability and the molecular organization of nodes of Ranvier. *J. Neurosci.* *24*, 7230-7240.
97. Yang, Y., Ogawa, Y., Hedstrom, K.L., and Rasband, M.N. (2007). betaIV spectrin is recruited to axon initial segments and nodes of Ranvier by ankyrinG. *J. Cell Biol.* *176*, 509-519.
98. Zamvil, S., Nelson, P., Trotter, J., Mitchell, D., Knobler, R., Fritz, R., and Steinman, L. (1985). T-cell clones specific for myelin basic protein induce chronic relapsing paralysis and demyelination. *Nature* *317*, 355-358.

99. Zhang, X., and Bennett, V. (1998). Restriction of 480/270-kD ankyrin G to axon proximal segments requires multiple ankyrin G-specific domains. *J. Cell Biol.* *142*, 1571-1581.
100. Zhou, D., Lambert, S., Malen, P.L., Carpenter, S., Boland, L.M., and Bennett, V. (1998). AnkyrinG is required for clustering of voltage-gated Na channels at axon initial segments and for normal action potential firing. *J. Cell Biol.* *143*, 1295-1304.
101. Zonta, B., Desmazieres, A., Rinaldi, A., Tait, S., Sherman, D., Nolan, M., and Brophy, P. (2011). A Critical Role for Neurofascin in Regulating Action Potential Initiation through Maintenance of the Axon Initial Segment. *Neuron* *69*, 945-956.

Vita

Nicholas Matthew George was born in Pittsfield, Massachusetts in April 1991. He graduated from Taconic High School in Pittsfield, MA in 2009, and received a Bachelor of Science in Human Nutrition, Food, and Exercise from Virginia Polytechnic Institute and State University (Virginia Tech) in 2012.